UNIVERSIDAD TÉCNICA FEDERICO SANTA MARÍA

DEPARTAMENTO DE FÍSICA

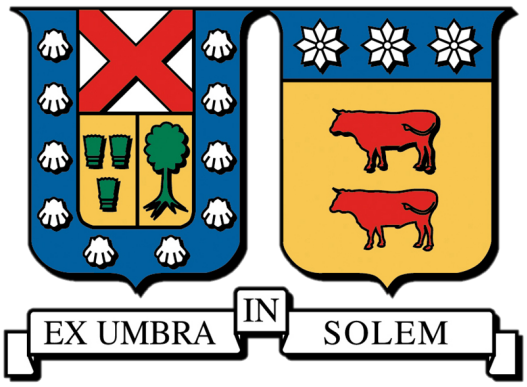

J194827-131733: A new eclipsing magnetic cataclysmic variable

Joaquín Meza Lagos

MEMORIA PARA OPTAR AL TÍTULO DE LA LICENCIATURA EN ASTROFÍSICA

PROFESSOR: Odette Toloza

March 7, 2024

Abstract

Cataclysmic Variables (CVs) are binary star systems composed of a main sequence star that donates material to a white dwarf companion, which acts as the accretor, typically within an accretion disk. However, when the white dwarf possesses strong magnetic fields, the formation of a disk is prevented, resulting in systems known as polars. Here, I present the discovery of a polar CV in this study.

As part of the observational program of CVs using ESO Xshooter, I observed the system J194827-131733. During a 3.5-hour observation period, 81 spectra were captured, which I applied telluric correction with *Molecfit* in the VIS arm. This large dataset is combined with the long term high cadence *TESS* photometry, I perform a deep analysis on this system. The Lomb-Scargle periodogram of the *TESS* light curve revealed a principal orbital period of 5.197 ± 0.015 hours, with other significant peaks being harmonics of the principal.

The system displays distinct characteristics indicative of being an eclipsing polar CV: (1) Notable He II emission lines in its spectrum, likely originating near the white dwarf rather than from the irradiated hemisphere of the donor stars, (2) the absence of double-peaked emission lines, suggesting the lack of an accretion disk, and (3) single periodicity.

The creation of trailed spectra suggests a configuration where the donor star is heavily irradiated by the white dwarf, and accretion likely follows a ballistic stream. There is speculation that the accretion curtain lies along the line of sight. Additionally, unlike many polars where He II emission emanates from the irradiated face, in this system, the emission is predominantly produced near the white dwarf, similar to the asynchronous polar BY Cam.

The discovery of this polar system, previously uncatalogued, unveils unusual parameters, including one of the longest orbital period, and significantly higher luminosity compared to known polar CVs. Therefore, this is an interesting system for multi-wavelength follow up studies.

Acknowledgments

I am profoundly grateful to my professors at the University, with special recognition to my mentor, Professor Odette Toloza, for her invaluable contributions and unwavering support throughout this project. Professor Odette's guidance, expertise, and encouragement have been pivotal in navigating the complexities of this endeavor, leading to its successful completion. Additionally, I am deeply appreciative of the opportunity to conduct observations at Paranal, which has greatly enriched my academic experience.

I want to thank my family, partner, friends, and colleagues for always having my back during this project. Their support and encouragement meant the world to me. Studying alongside my colleagues and having my family's constant support were invaluable throughout this journey. I'm grateful for their unwavering presence and understanding.

Contents

Chapter 1

Introduction

This thesis project emerges from an extensive observational program employing X-shooter with the primary goal of surveying all CVs within a 300 pc radius. The overarching objective is to enhance a census previously conducted within a 150 pc range (Pala et al., 2020). With the purpose to acchieve a statistically significant CV sample. The initial sample within the 150 pc radius comprises a limited population of CVs, yielding only 15 mCVs. A comprehensive and statistically significant census presents a unique opportunity to validate our synthetic population model based on the standard CV model (e.g. Knigge et al., 2011; Belloni et al., 2018; Schreiber et al., 2015).

We will focus our investigation in this work on a specific system from this program that I observe with X-shooter, with the name J194827-131733. This system exhibits distinctive features characteristic of a mCV. As a theoretic introduction we will discuses fundamental elements of CVs, with a specific focus on mCVs, followed by an explanation of the method section, which includes a detailed technical description of X-shooter, specifics of the observation run, and the implementation of MOLECFIT for the telluric correction. The results section will showcase the trailed spectra of the system, and presents our proposed accretion model for J194827-13173. Finally, I discuss and conclude about the results by the end of this work.

1.1 Concepts in Binary systems

1.1.1 Roche lobe geometry

In a binary system, the two stellar components exist within a rotating frame of reference where the presence of centrifugal force alters the gravitational potential. This combined potential, known as the Roche potential, arises from the interplay of centrifugal and gravitational forces. Near each stellar surface, where the gravitational potential of one star predominates, the equipotential surfaces of the Roche potential are spherical. However, as one moves away from the stars where centrifugal force becomes more influential, these surfaces become ellipsoidal. The innermost equipotential surfaces encompassing both stars are termed Roche lobes. In Figure 1.1, the bottom level illustrates the equipotential lines. Notably, L_1 serves as a stable saddle point. If mass overflows the L_1 point, the material can move freely towards the companion, crossing the L_1 point (namely Roche Lobe overflow).

Based on if one or two stars fill their Roche Lobe, there exist three cases for binary systems:

- **Detached binaries:** The two stars do not fill the Roche Lobe.
- **Semi - detached binaries:** One star fill its Roche Lobe and begins mass transfer to the other that have not filled the Roche Lobe.[1]
- **Contact Binaries:** Both stars fill the Roche Lobe

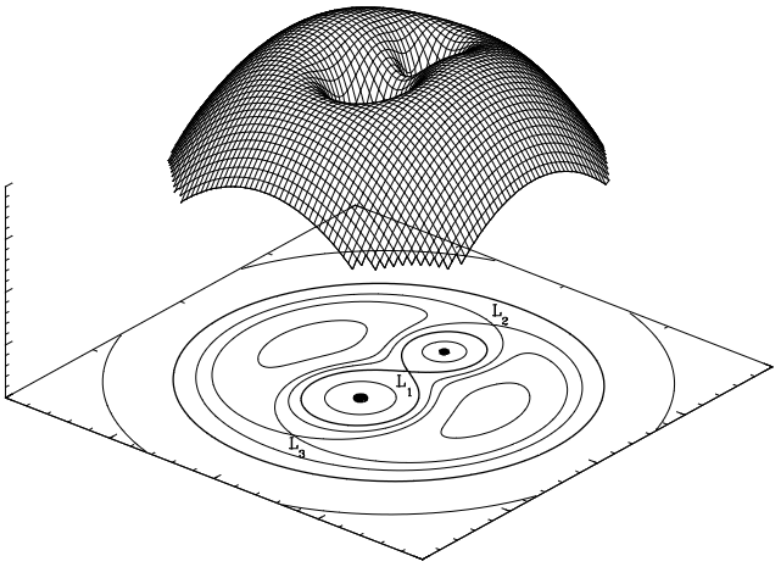

Figure 1.1: Binary system co rotating potential energy. The the bottom plane displays a contour plot where the lines are equipotential. L1 is the stable lagrangian point, and L2 and L3 are unstable lagrangian points.

1.1.2 Types of mass transfer

The Roche Lobe represents the final level surface within a binary system that ensures all mass remains gravitationally bound to one of the stars. If a star expands beyond its Roche Lobe boundaries or if the Roche Lobe contracts due to orbital angular momentum loss, it can result in the star filling its Roche Lobe. This overflow of mass compels material to transfer to the other star in the binary system.

Ones the Roche lobe is overflow exist a mass transfer process, this mass transfer have different types in which I will discuss briefly (for a review see Belloni & Schreiber 2023)

The stability of mass transfer through Roche Lobe filling is a consequence to fact that the secondary star can no longer be regarded as evolving in isolation. Its internal structure may undergo adjustments due to the process of mass loss. Stable mass transfer occurs when the star has sufficient time to readjust to the lost mass, contingent upon the response of its radius to the mass loss. In essence, if the hydrodynamical timescale is shorter than the mass loss timescale, then stable mass transfer ensues.

[1]This is the case of CVs. Where the Donor Star is a MS that transfer material to the WD

Dynamical timescale mass transfer

I will define two important quantities for mass transfer process, one is the adiabatic radius–mass exponent express in equation (1.1), refers to logarithmic derivate of the radius of the donor respect to the mass of the donor .

$$\zeta_{ad} = \left.\frac{\partial ln R_d}{\partial ln M_d}\right|_{ad} \tag{1.1}$$

And the other is Roche Lobe radius–mass exponent (eq. 1.2). refers as the logarithmic derivative of the Roche Lobe radius respect to the donor's mass.

$$\zeta_{RL} = \frac{\partial ln R_{RL}}{\partial ln M_d} \tag{1.2}$$

Hence, to maintain the donor star in hydrostatic equilibrium, it is essential for the difference between the adiabatic and Roche Lobe radius-mass exponents to be positive. Essentially, through comparing these two derivatives, we can ascertain whether the donor's inner layers respond to mass transfer adiabatically. This means that the entropy profile within the stellar interior remains unchanged despite the loss of mass. Conversely, if $\zeta ad < \zeta_{RL}$, indicating that the adiabatic exponent is less than the Roche lobe exponent, mass transfer becomes unstable. In such cases, mass transfer occurs on a *dynamical timescale*, as the mass transfer rate is solely constrained by the sonic expansion of the envelope through the inner Lagrangian point.

Thermal time-scale Mass Transfer

The thermal equilibrium of a star, characterized by the balance between nuclear energy generation and atmospheric radiation losses.

Under a stable mass transfer process, maintaining hydrostatic equilibrium, the next question is, must it compromise its thermal equilibrium to confine its surface within the Roche Lobe?.

If the donor's interior is afforded sufficient time to adjust and attain thermal equilibrium, stable thermal mass transfer ensues as indicated by equation (1.3). Conversely, if the mass transfer timescale surpasses the thermal timescale, the mass transfer becomes thermally unstable.

$$\zeta_{eq} = \left.\frac{\partial ln R_d}{\partial ln M_d}\right|_{th} \tag{1.3}$$

To compute ζ_{eq}, the mass-radius relation for stars in thermal equilibrium must be known. If mass transfer is dynamically stable, it will also be thermally stable if $\zeta_{eq} > \zeta_{RL}$. In this case, mass transfer needs to be driven by an external process and proceeds on a time-scale different from the dynamical and thermal time-scales. On the other hand, if $\zeta_{ad} > \zeta_{RL} > \zeta_{eq}$, mass transfer will be driven by thermal readjustment and proceed on the donor thermal time-scale.

1.2 Cataclysmic variables

Cataclysmic Variables (CVs) represent binary systems characterized by the interaction between a main-sequence (MS) donor star, typically of a low mass non-degenerate M-type, and a white dwarf (WD) companion acting as the accretor. The mass transfer mechanism comes into play when the

Roche Lobe, is filled. Subsequently, the MS star initiates the transfer of material onto the WD. In cases where the WD lacks a magnetic field presence, this process results in the formation of an accretion disk.

1.2.1 Formation and evolution of CVs

The progenitors of CVs are detached binary systems where the more massive star, having exited the main sequence earlier, fills its Roche Lobe during either the first giant branch or asymptotic giant branch phase. Subsequently, the system undergoes a phase of unstable mass transfer from the more massive primary to the less massive secondary, leading to the evolution into a common envelope configuration, with the primary's envelope encompassing both stars. Following the expulsion of the envelope, a close, short orbital period detached Post-Common Envelope Binary (PCEB) remains. This PCEB consists of the core of the giant primary, which evolves into a white dwarf, and a low-mass secondary star.

Due to subsequent losses in angular momentum via mechanisms such as magnetic braking (MB, stemming from a stellar wind associated with the secondary's magnetic activity, as described in Section 1.2.2) and gravitational wave radiation (GWR, as explained in Section 1.2.2), causes the orbit to shrink over time, and thus the PCEBs transition into a semi-detached configuration, ultimately evolving into a CV.

1.2.2 Angular momentum loss mechanisms

The evolution of binary star systems is primarily governed by angular momentum loss, which manifests through two principal mechanisms: magnetic braking and gravitational radiation. As angular momentum dissipates from the system, a mechanical consequence emerges: the orbit contracts. In essence, the system loses energy, causing the stars to draw closer to each other. And by Kepler law the orbital period shrinks to P_{orb}.

Magnetic Braking

Magnetic braking occurs when a stellar wind (Verbunt & Zwaan, 1981), slightly magnetised due to the star's magnetic field, is forced to follow the lines of that magnetic field. This wind, charged with electricity, escapes into outer space from the star's poles. As the magnetic field lines co-rotate with the star, they carry away some of its angular momentum, causing the star's rotation to slow down (Schatzman, 1962; Kraft, 1967). However, in compact binary systems, the secondary star is tidally locked, meaning its rotation rate matches the orbital period.

This results in the removal of angular momentum from the system, causing the orbital period and separation to decrease, and consequently, the secondary star spins up as it moves in tighter orbits. The origin of the stellar magnetic field, which is essential for magnetic braking, is uncertain but is believed to arise from a dynamo effect in the tachocline, the region between a star's radiative core and convective envelope (MacGregor & Charbonneau, 1997; Charbonneau & MacGregor, 1997).

The effectiveness of magnetic braking depends on the intensity and configuration of the magnetic field. When the secondary star's mass is around 0.2 to 0.3 times that of the Sun, it becomes fully convective, leading to a significant reduction in the magnetic field intensity and changes in

its topology. This reduces the efficiency of magnetic braking by closing the field lines at the stellar surface, hindering the escape of the stellar wind and reducing angular momentum removal (Knigge et al., 2011).

Despite its importance, magnetic braking is poorly understood and challenging to model accurately due to incomplete understanding of its underlying physics. A review of all available prescriptions is presented in Knigge et al. (2011).

Gravitational Radiation

Binary systems emit gravitational waves, which carry energy away and cause the two stars to spiral inward. These distortions in space-time were predicted by Einstein in his General Relativity Theory in 1916, and their existence has recently been confirmed by experiments such as the Laser Interferometer Gravitational-Wave Observatory (LIGO) and Virgo (Abbott et al., 2016b,a). These experiments have detected gravitational waves originating from black holes. The rate at which gravitational wave radiation (GWR) removes angular momentum from a system can be precisely calculated using the theory of General Relativity (Paczyński, 1967). GWR continuously affects every binary system and plays a significant role in causing the orbit to shrink, particularly in compact binaries like double white dwarfs, double neutron stars, and neutron star plus black hole binaries. As the orbital separation decreases, the efficiency of GWR increases because the rate of angular momentum loss is inversely proportional to the separation.

However, GWR is less efficient than magnetic braking (MB). In CVs, GWR only becomes dominant for CVs with orbital period less than 2-3 hours, when the orbital separation is smaller, and MB has been significantly reduced due to the transition of the secondary star into a fully convective state.

1.2.3 Classification of CVs

CVs are initially classified based on the presence or absence of a magnetic field, leading to two main categories: non-Magnetic CVs and Magnetic CVs (mCV).

For the non-Magnetic CVs a secondary classification: Dwarf Novae and Nova (See Balman 2020 for a recent review): The former, the Dwarf Novae exhibit periodic changes in luminosity attributed to disk outbursts, as proposed by Osaki (1974). This phenomenon is driven by a continuous mass transfer process, leading to the accumulation of material in the accretion disk. The persistent mass inflow induces a build-up in disk viscosity, triggering an enhancement in angular momentum transfer. Consequently, this heightened transfer of angular momentum results in a rapid accretion of material onto the white dwarf, leading to a surge in luminosity. Then the disk forms again because of the constant mass transfer from the donor, and the cycle starts again. The latter, the novae, display Nova eruptions, which represent the most dramatic events in CVs. While Dwarf Novae outbursts exhibit a brightness change of 3-5 magnitudes, Nova events are characterized by a more substantial change in brightness, ranging from 8-15 magnitudes (Warner, 1995). This process involves nuclear reactions occurring in the layer where the white dwarf accretes material. The hydrogen within this accreted layer, influenced by the gravitational forces of the WD, becomes degenerate. As additional material flows onto the white dwarf, the density increases. In a degenerate environment, the energy released by nuclear reactions does not elevate the pressure. Instead, the temperature rises, facilitating more efficient nuclear reactions, leading to a runaway

process. Nova CVs can be further classified into recurrent, which have demonstrated multiple instances of brightness changes indicative of a nova eruption, and Classical Nova, characterised by a singular episode of nova eruption.

In contrast, mCVs have a secondary classification is established to distinguish between systems with varying strengths of magnetic fields (Ferrario et al., 2015). Specifically, Polar Systems exhibit a strong magnetic field (i.e 10-80 MG), while Intermediate Polars are characterized by an intermediate strength of the magnetic field (i.e 1-10 MG) associated with the WD, for a review see (Mukai, 2017). This work focus on a magnetic CV system, and therefore more details about magnetic CVs are given the following section 1.3.

1.3 Magnetic Cataclysmic Variables

Magnetic fields influence the motion of charged particles, leading to a complex interplay, especially when considering that accelerating charged particles also generate magnetic fields, creating a intricate feedback loop.

Typically, the system is divided into two distinct regions. In the first region, the magnetic field is relatively weak, unable to dictate the trajectories of particles. Consequently, particles follow their paths independently. Conversely, in the second region, where the magnetic field is sufficiently strong, it induces all particles to align with magnetic lines and co-rotates with the WD. This specific region is referred to as the *Magnetosphere*. The interpretation of this dynamic involves acknowledging a transition zone where both processes play a significant role.

Material within the magnetosphere accretes over the poles of the WD, forming a concentrated stream. The potential energy of this material is transformed into kinetic energy, culminating in the stream colliding with the WD surface, creating an "accretion shock" (Imamura et al. (1987)). This process generates X-ray emission due to the conversion of kinetic energy. Notably, the elevated temperature of the feeding stream is proficient in ionising helium twice. Consequently, a salient characteristic mCVs is the presence of He II emission lines (Schwarz et al., 2005, e.g.).

Typically, a fundamental differentiation is made between a narrow emission line (NEL) attributed to the secondary star and a broader underlying component believed to originate somewhere within the accretion stream. This distinction is commonly referenced in literature, such as in the works of Liebert & Stockman (1985) and Biermann et al. (1985), both leads to the same conclusions, the irradiated hemisphere of the donor emits NEL meanwhile the broad emission lines are from the stream.

1.3.1 Detecting of magnetic field in white dwarfs

Cyclotron Humps

The magnetic flow tracing a magnetic field line does not exhibit a linear trajectory; instead, it displays a helical symmetry. This phenomenon arises from the behaviour of charged particles, resembling a current. When a current moves perpendicular to a magnetic field line, it undergoes a force perpendicular to both the magnetic field and the current direction, inducing circular motion. Incorporating the gravitational effect, which augments the velocity in the current direction, results in a helical path akin to a spring emitting polarised light (Cropper (1990)).

Since accelerating charged particles are emitting photons, and a circular motion involves constant acceleration this type of radiation is called *Cyclotron Emission*. This emission exhibits harmonic frequencies, manifesting as equally spaced humps in the spectrum, commonly referred to as *Cyclotron Humps*.

Polarimetry

In ordinary circumstances, an oscillating electron can align itself in any direction, leading to emitted light photons propagating perpendicular to the electron's trajectory. However, when the vectors of photons align in a specific direction, the resulting radiation is termed as linearly polarized. Now, envision observing the field lines directly facing them: the electron, tracing a spiral path, appears to circle and emit photons perpendicular to its trajectory. This phenomenon characterizes circularly polarized light.

The connection between polarized light and the strength of the magnetic field of a white dwarf emerges from the electron's spiral path. Barrett & Chanmugam (1984) devised a method to gauge the magnetic field's strength by examining the ratio of circular polarization to linear polarization in the emitted light. This approach provides a means to estimate the magnetic field intensity through the polarization characteristics of the radiation.

Zeeman effect

Zeeman splitting in white dwarfs refers to the phenomenon where the spectral lines emitted by atoms in the WD atmosphere split into multiple components due to the presence of a magnetic field. This effect arises because the energy levels of the atoms are modified by the magnetic field, causing the spectral lines to shift. The strength of the magnetic field determines the extent of the splitting: stronger fields lead to larger separations between the components.

In low state, when the WD it is observable it is possible to measure the Zeeman effect, therefore calculate the magnetic field that produce it. It was possible to use this method to measure the magnetic field of a low state polar (e.g. AM Her, Latham et al., 1981; Patterson & Price, 1981).

1.3.2 Polar CVs

Polar CVs have typical magnetic fields ranging from 10 to 80 MG, the accretion stream initially remains unaffected by the magnetic field, tracing a trajectory as it would in a non-magnetic system until it nears the WD. As long as the magnetosphere extends beyond the circularization radius, the stream cannot freely orbit and, consequently, does not form a disk. When the magnetic field gains dominance, the stream alters its direction, necessitating it to flow out of the plane and follow the magnetic field lines for the remainder of its journey.

In Fig 1.2, we present an illustrative case depicting a polar CV characterized by ballistic accretion, ultimately dominated by the magnetic field of the WD (Kotze, E. J. et al., 2016). The blue lines in the figure represent streams tracing magnetic field lines within the magnetosphere. In this magnetospheric region, particles undergo acceleration, contributing to the formation of the He II emission line. Subsequently, when these streams impact the WD surface, X-ray emission is generated (Mukai, 2017).

Polar CVs frequently exhibit an irradiated hemisphere originating from the donor star. This phenomenon occurs due to the lack of an obstructing stream that would otherwise impede the

white dwarf radiation (Schmidt et al., 1995). Within this irradiated region, narrow emission lines of H_β and He II (Biermann et al., 1985) are commonly observed. These emission lines serve as prominent indicators of the intense irradiation that emits the WD.

The L_1 Lagrangian point introduces friction to the material passing through, leading to a temperature increase at this point and a corresponding enhancement in brightness—commonly referred to as the bright spot. Another significant region is the elongated section of the donor, where accelerating particles give rise to a ballistic stream, creating another zone of heightened luminosity.

There are two important periods to study en mCVs, the orbital period and the spin period of the WD. If the WD present a strong magnetic field (polar CVs) provoke a lock the primary into synchronous rotation with the binary orbit and to prevent completely an accretion disc from forming (for a more detailed explanation see Hellier 2001.)

Few polar systems have white dwarf which have asynchronous rotations to the orbital periods (e.g. Kolbin et al., 2024; Littlefield et al., 2019; Halpern, 2024). It has been measured that the white dwarf spin period is lower than the orbital period (Littlefield et al., 2023). Another evidence is important to mention, the light curve period is different to the period of X-ray. This indicates that the accretion stream alternate between the two poles of the WD. This usually defines as the beat period ($\omega_{beat} = \omega_{spin} - \omega_{orb}$), and it could be find as a peak in a periodogram of a light curve or as a periodic decay of flux of emission lines, representing the change of accretion pole.

Throughout a single beat cycle, the accretion flow originating from the secondary star revolves around the magnetic field of the white dwarf. In other words, the alignment of the WD's magnetic field relative to the secondary star repeats itself at the beat period. The accretion flow's behaviour is contingent upon the orientation and geometry of the magnetic field. Consequently, it may follow varied magnetic field lines and possibly transition from one pole to another.

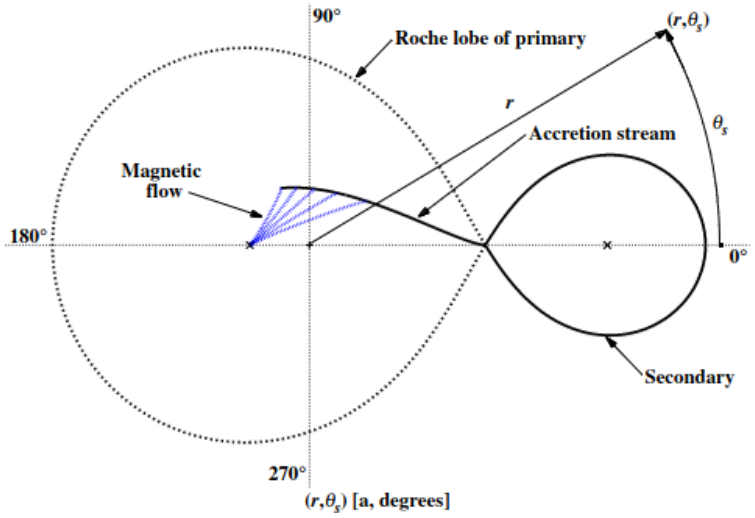

Figure 1.2: Representtion of a Polar CV in polar coordinates. r is the distance of the C.O.M and θ_s is the polar angle. The secondary is the donor (red dwarf Main Sequence Star), the primary is the WD. Figure taken from Kotze, E. J. et al. (2016)

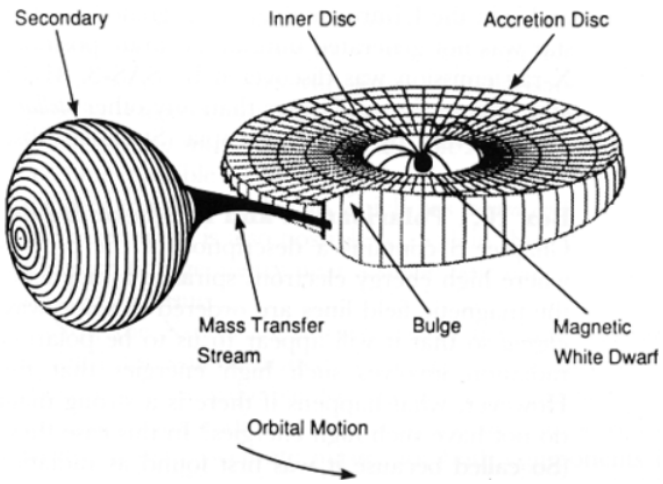

Figure 1.3: Intermediate Polar diagram, in which we can observe a accretion disk that is disrupted in the inner disc in which the magnetic field is enough to force to move the particles through magnetic lines, and falling into one pole.

1.3.3 Intermediate Polar CVs

Intermediate Polar have asynchronous rotations $\frac{P_{spin}}{P_{orb}} < 0.6$ due to magnetic field is a too weak to lock the system, or the separation is too large.

The strength of the magnetic field of the WD affect the grade of disruption of the disk (see figure 2.1). Typically the strength of the magnetic field in intermediate polar is in the range between 1-10 MG (let's recall that polar systems have 10-80 MG). IP show double peaked emission lines due to the accretion disk Beuermann & Reinsch (2008).

In certain cases, IPs have the potential to evolve into polar systems through AML. This evolutionary process results in the shrinking of the orbit, possibly leading to a scenario where the WD's magnetic field becomes sufficiently strong to lock the secondary star. Consequently, it becomes more probable to encounter polar systems characterised by shorter orbital periods.

1.3.4 Low to High State Variations in Polar Systems

Some CVs with magnetic fields display significant brightness variations of approximately ~ 3 magnitudes over extended time-scales (i.e. on time-scales of many epochs of P_{orb}; e.g. Kalomeni 2012). The durations of such states range from days to years and occur at irregular interval. The period of heightened luminosity is conventionally denoted as the "high-state", contrasting with the phase characterised by reduced luminosity, named the "low-state" (i.e Shears 2021 and in the left panel in Figure 1.4 an example is shown). mCV in low state permit to observe the white dwarf due to the decay of the accretion stream.

Evidence indicates the presence of star spots on the secondary MS star, as demonstrated by Webb et al. (2002), who observed TiO absorption lines. These spots on the secondary star influence the mass transfer rate, causing a reduction when the spot obstructs the face involved in material transfer. It is thought that low and high state variations are relate to mass transfer, accretion disc and orbital period Howell (2004) but a complete explication remain unclear. A example of the polar system AM Her, which transitions from high and low state and viceversa is shown in 1.4.

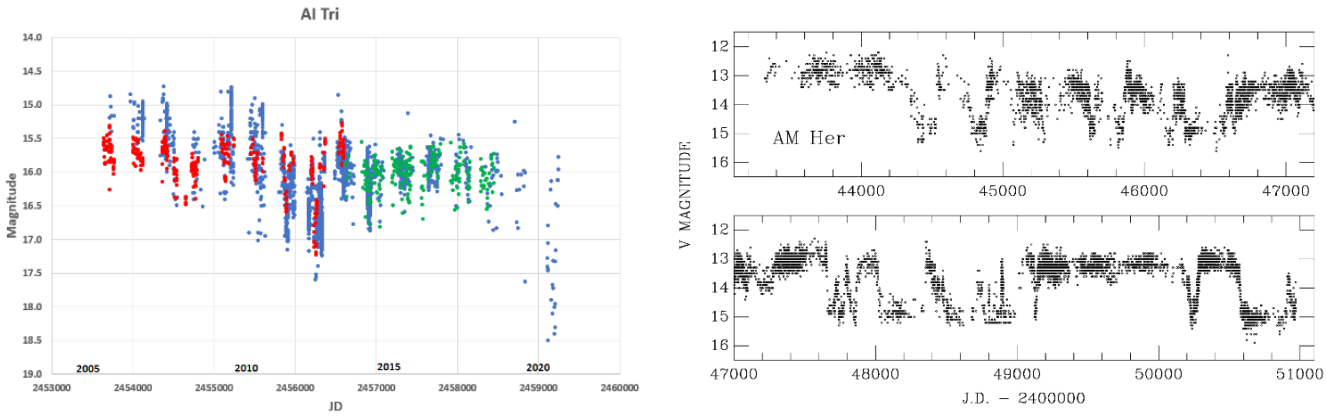

Figure 1.4: Examples of low states in 2020 found by Shears (2021) in Al Tri (right), and AM Her transition in to high and low state (left; Hessman et al. 2000)

For mCVs, polars exhibit notable high and low states, whereas low states are less common in IPs, however there have been reported few systems presenting low state (Warner, 2003).

Chapter 2

Methods

To model J194827-131733, our approach involves leveraging photometric data from *TESS* and *Gaia* surveys, coupled with spectrographic observations obtained through Xshooter. *TESS* provides light curves permitting the extraction of the system's orbital period, because J194827-131733 is a eclipsing CV then using a periodogram we find the orbital period of the system. While Gaia monitoring reveals if a transition of high to low states occur. Incorporating the spectroscopy, we intend to utilise the TESS-derived period to fit trailed spectrum lines, finding the orbital phase of the distinctive lines, contrasting our results with established polar models (refer to Section 1.2.3). This comprehensive strategy integrates various observational sources to refine our understanding of the new discover mCV J194827-131733.

2.1 Determining the orbital period from *TESS*

The space telescope Transiting Exoplanet Survey Satellite (*TESS*, Ricker et al. 2014) have provided new opportunities for studies of CVs by providing high-cadence photometric data over an extended time base. *TESS* stands out a powerful tool to determine periodicities of variable object, permitting to investigate the period of eclipsing CV, i.e. the system J194827-131733. The finding chart of J194827-131733 is shown in Figure 2.1, displays the aperture used to perform the photometry to build the lightcurve by the automated SPOC pipeline. *TESS* monitoring period for J194827-131733 ranges from 2022-07-09 09:43:08.574895 UTC to 2022-08-04 15:12:55.726993 UTC.

We retrieved the light curve data from the *TESS* mission using the free PYTHON package LIGHTKURVE version 2.4.2. A log of the data specified in Table 2.1. The light curve is displayed in Figure 2.2, where the flux corresponds to the PDCSAP_FLUX column. This flux represents the corrected output flux obtained after processing the observations through the *TESS* pipeline, which accounts instrumental errors, and systematic errors. The x-axis of the plot represents Barycentric *TESS* Julian Days (BTJD). *TESS*, being a space telescope, moves through space, causing variations in the distance between the source and the telescope over time. To correct these variations, we utilize the barycentric correction, that is a *TESS* column in JD that incorporate the relative distance variations of *TESS* over time.

The light curve of J194827-131733 displays periodic decreases in brightness observed, which are attributed to eclipses occurring within the system. The periodogram of this light curve is shown in Figure 2.3. The power spectral density of a signal (in terms of series) show the peak

Figure 2.1: Background image is *gri* combined images of Pan-STARRS survey. The object at the center (marked which a red cross) is the system J194827-131733. Overplotted is the aperture used to extract the photometry of the source. The other two stars circled in the field are additional objects for which *TESS* has measured their brightness.

Table 2.1: *TESS* information of J194827-131733

Mission	Year	Author	Exposure Time (s)	Target Name	CROWSAP	FLFRCSAP
TESS Sector 54	2022	SPOC	120	47780469	0.60431617	0.56354576

points, which represent frequency of potential periodic signals. To assess the significance of peaks in our periodogram, we employ the false alarm probability library provided by Astropy[1] (Astropy Collaboration et al. (2022)), utilizing the BOOTSTRAP method. False alarm probability quantifies the likelihood of the peaks being spurious periodic signals and assigns a probability accordingly. Various methods exist for calculating this probability, with one such method being the bootstrap approach. This method relies on simulations and is computationally expensive. The procedure involves randomly shuffling the array of the light curve and computing the periodogram of the shuffled array. This process is repeated multiple times. Subsequently, the signals obtained in the original periodogram are compared with those from the shuffled periodograms. If a peak is significant, its false alarm probability will be low.

In our analysis, we set a false alarm probability threshold of 0.01%, as illustrated with a red dashed line in the left of the Figure 2.3. Peaks above this threshold represent periodic signals with a 99.99% probability. This approach ensures a rigorous assessment of the significance of periodic signals detected in the periodogram. By setting a stringent threshold, we mitigate the risk of false positives and enhance the reliability of our findings.

I identified several significant peaks, however the high peak in the periodogram corresponds to the orbital period. $P_{orb} = 5.197 \pm 0.015$ hr. The other peaks are equally spaced in frequency,

[1] https://docs.astropy.org/en/stable/timeseries/lombscargle.html

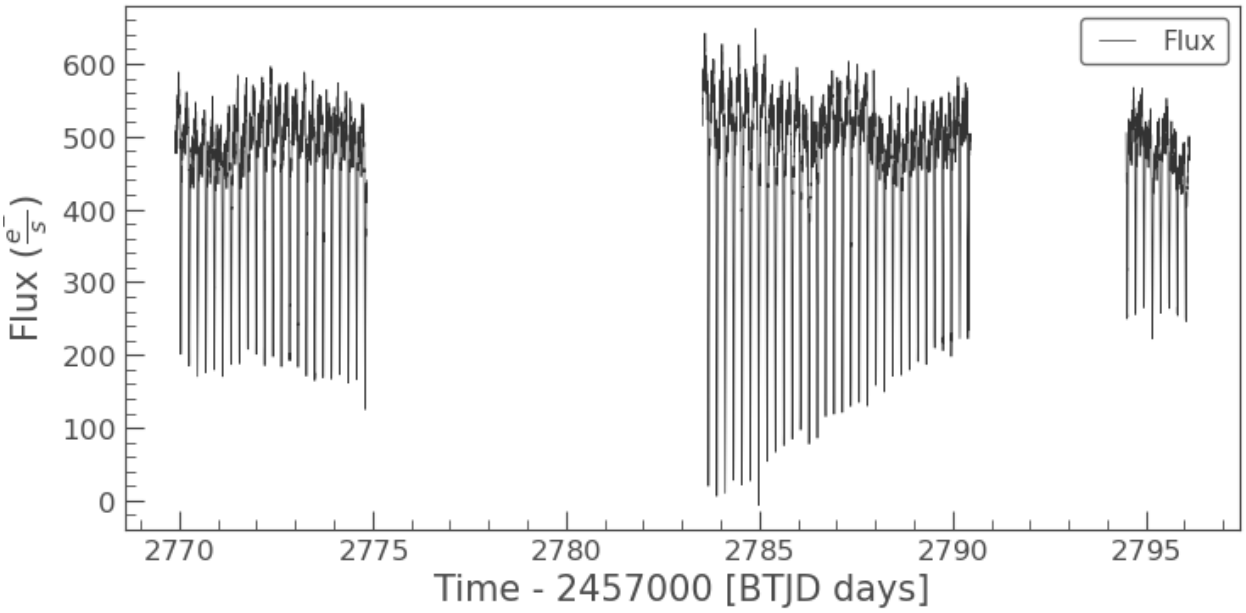

Figure 2.2: *TESS* light curve of J194827-131733, which displays clear and sharp eclipses.

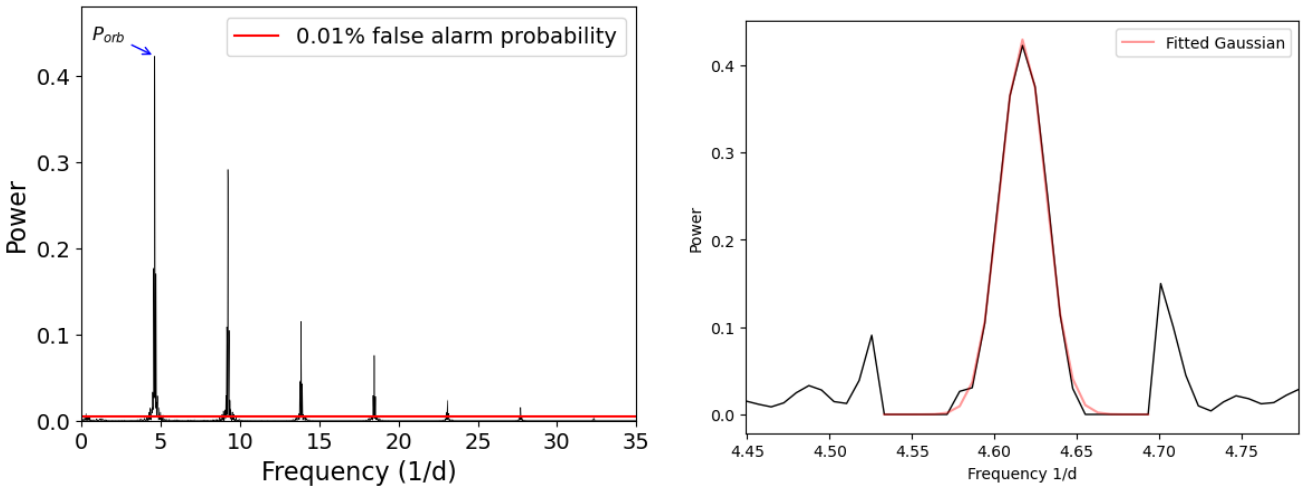

Figure 2.3: *Left* Periodogram of TESS light curve where the the highest peak corresponds to $P_{orb} \approx 5.197 \pm 0.015\ hr$. *Right* Gaussian fit to the maximum peak of the periodogram to extract a standard deviation in the frequency space, i.e. the error of the orbital period.

probably are only harmonics of the principal period. To estimate an error on the orbital period measurement, I performed a Gaussian fit to the maximum signal in the right image of Figure 2.3.

The FLFRCSAP (Table 2.1) has a value of 0.56354576. From this value, we see that the aperture contains only 56% of the object's flux, and the difference of the flux in the aperture is due to other objects therefore the periodicity measured might not correspond to the flux of the J194827-131733. To asses if the period I measured corresponds to J194827-131733, I asked kindly to Mercedes Hernandez use the TESS_LOCALIZE[2] tool. This tools involves determining the

[2] https://github.com/Higgins00/TESS-Localize

position of a variable source in the sky and identifying the most probable *Gaia* source based on *TESS* pixel data and observed frequency variations (Higgins & Bell, 2023). The tool provides a likelihood of 100% (p-value of 0.2540701).

The analysis of the TESS light curve suggests that we are observing an eclipsing mCV. The periodogram analysis reveals a prominent peak at approximately $P_{\rm orb} = 5.197 \pm 0.015\ hr$, accompanied by a low false alarm probability. This characteristic peak is indicative of the orbital period of the system.

TESS_LOCALIZE implementation confirm that the flux variations originate from the source J194827-131733 detected by TESS. This tool provided a probability of 100% that the observed flux variations indeed originate from J194827-131733. This high probability reinforces our confidence in the association between the observed flux variations and the identified source.

Extrapolating the TESS light curve up to the time of the observations of J194827-131733 enables the realization of phase-resolved spectroscopy. This facilitates a comprehensive analysis by integrating our observations with X-shooter data and the TESS light curve.

2.2 Spectroscopy with X-shooter on the VLT

J194827-131733 was observed as part of a large program of research of CV. The purpose of the program is to enlarge the current volume limited sample of 150 pc (i.e. 42 systems: Pala et al. 2020) such that it has a statistical significant size to make studies of the CV population of representative samples of the subclasses. Therefore, huge efforts have been made to observe all CV candidates within 300 pc, and the program 111.24UQ.001 with X-shooter aimed to observed 13 candidates to CVs. The observations were split into two visitor mode runs, in which I performed the observations of the second run attending to Paranal in person during September, 2023. Before explaining the analysis to the X-shooter spectra, I will briefly explain the X-shooter instrument, to carry on with the analysis of the spectra.

2.2.1 X-shooter technical specifications

X-shooter is a Echelle spectrograph within a 8 meter mirror of the VLT. The primary function of an Echelle Spectrograph is to disperse incoming light into its component wavelengths, creating a spectrum. The Echelle grating disperses light in the horizontal direction, while a cross-disperser (often a prism or another grating) disperses it in the vertical direction, more red wavelength are highest than blue ones (Figure 2.4). This results in a two-dimensional spectrum with many overlapping orders as we see in Figure 2.4, every arm have multiple Echelle Order vertically.

Utilizing an Echelle Spectrograph offers the distinct advantage of enhancing the wavelength range available for measurement. X-shooter, equipped with three arms—UVB, VIS, and NIR (see Table 2.2)—is particularly well-suited for studying CVs. Its design allows for simultaneous measurements across all three arms.

In practical terms, X-shooter facilitates the separate measurement of CV components. The WD component, predominantly observable in the UVB arm, can be distinguished from the MS star and the accretion disk, which exhibit greater brightness in the VIS and NIR arms. This capability enhances the precision and depth of observations in CV studies.

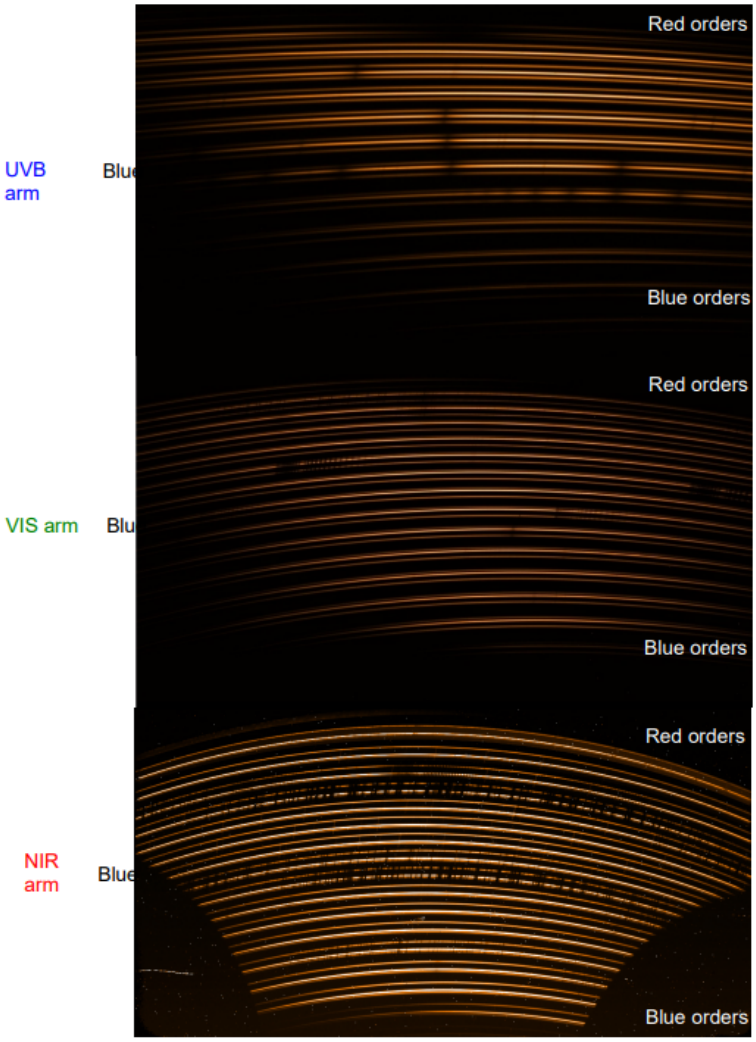

Figure 2.4: Xshooter spectrograph example, we can observe the three arms and the orders that constitute it (Image adapted from the X-shooter manual).

Table 2.2: Technical Description of Xshooter, readout mode for UVB and VIS is in fast readout with a binning of 2x2

Arm	**Wavelength range (nm)**	**Resolution (1" slit)**	N^{th} **order**	**Readout (s)**
UVB	300-550	5400	12	8
VIS	550-1000	8900	14	9
NIR	1000-2500	5600	16	0.88

2.2.2 Spectroscopy of the system J194827-131733

I took 81 spectra in the three arms for J194827-131733. The total time on-target is approximately 3 hours starting from 2023-04-26T06:18:58.644 to 2023-04-26T09:46:57.447. Given the flexure of instrument, it is advisable by ESO to operate the telescope no longer than 2 hours on-target.

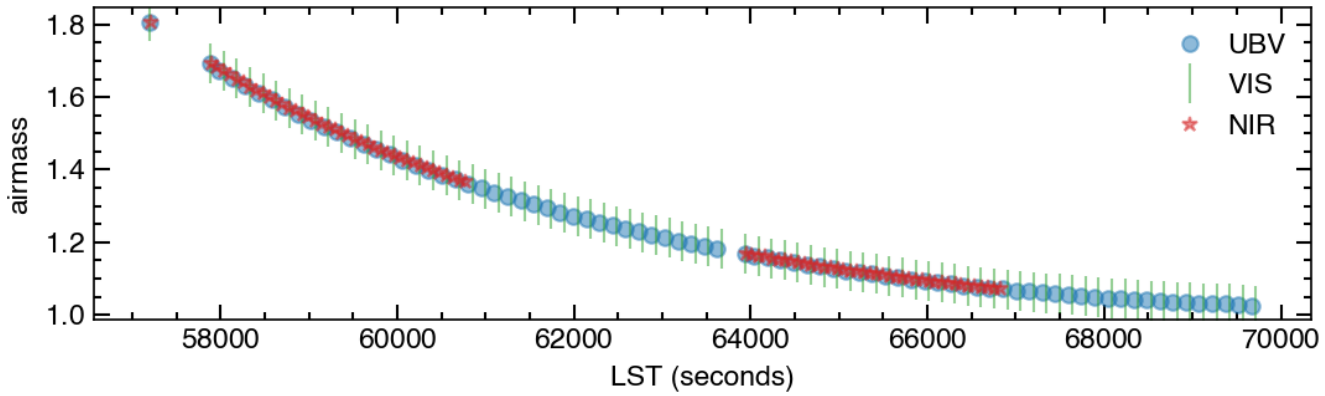

Figure 2.5: Adquisition of the 81 spectra long the local sideral time (LST) versus the airmass trough time, NIR exposure are disface of VIS and UVB due to its short readout time.

Therefore, the 81 spectra were taken in two sections. As the NIR arm boasts a quicker readout rate (see table 2.2), in contrast to the VIS and UVB arms, the successive spectra of UVB/VIS and NIR conclude earlier in the NIR segment. Consequently, while the VIS and UVB spectra span a longer timeframe compared to the NIR, they exhibit a delayed completion (See Figure 2.5). All the spectra have a exposure time of 60 seconds, in each of the X-shooter arms. Obtaining a mean airmass for UVB ≈ 1.24, VIS: ≈ 1.24 and NIR: ≈ 1.32

The object initially starts at a high airmass value of 1.8, attributed to its low altitude above the horizon. As time elapsed, the object ascended, resulting in a gradual reduction in airmass, eventually stabilizing at 1.0.

Initially, the X-shooter spectroscopy was attempetd to be reduced and calibrated using an universal PYTHON pipeline named PYPEIT[3]. Nevertheless, following a month of installation, learning, executing, and troubleshooting, I opted to abandon this pipeline and utilise the reduction pipeline offered by ESO instead (i.e. ESOREFLEX). The ESO portal[4] was used to retrieve the spectra and their associated raw calibration files. The input is the night of the observations and the PROGRAM ID: 111.24UQ.001. The raw data plus their associated calibration files are downloaded using the shellscript method. As a preparation of the dataset, I decompressed the files with the extension $*.Z$, as needed by the ESOREFLEX pipeline

ESOREFLEX is an environment that provides an easy and flexible way to reduce VLT/VLTI science data using the ESO pipelines. It is build using the Kepler workflow engine[5]. To illustrate the X-shooter spectra, the first of the spectra of J194827-131733 is shown in gray in Figure 2.6. In the spectra, notable emission lines include the Balmer lines, such as H_β and H_α, which appear prominently. Additionally, in the UVB arm, distinct single-peaked emission lines of He II are observed, while in the VIS arm, the Calcium Triplet stands out. These emission lines are distinctly labeled in red and will be the focal point of discussion in the trailed spectrum analysis.

But I would like to draw the attention to the bands of telluric absorption, which need to be removed.

The interaction of the light from astronomical objects with the molecules of the Earth's atmo-

[3] https://pypeit.readthedocs.io/en/release/
[4] http://archive.eso.org/eso/eso_archive_main.html
[5] https://kepler-project.org

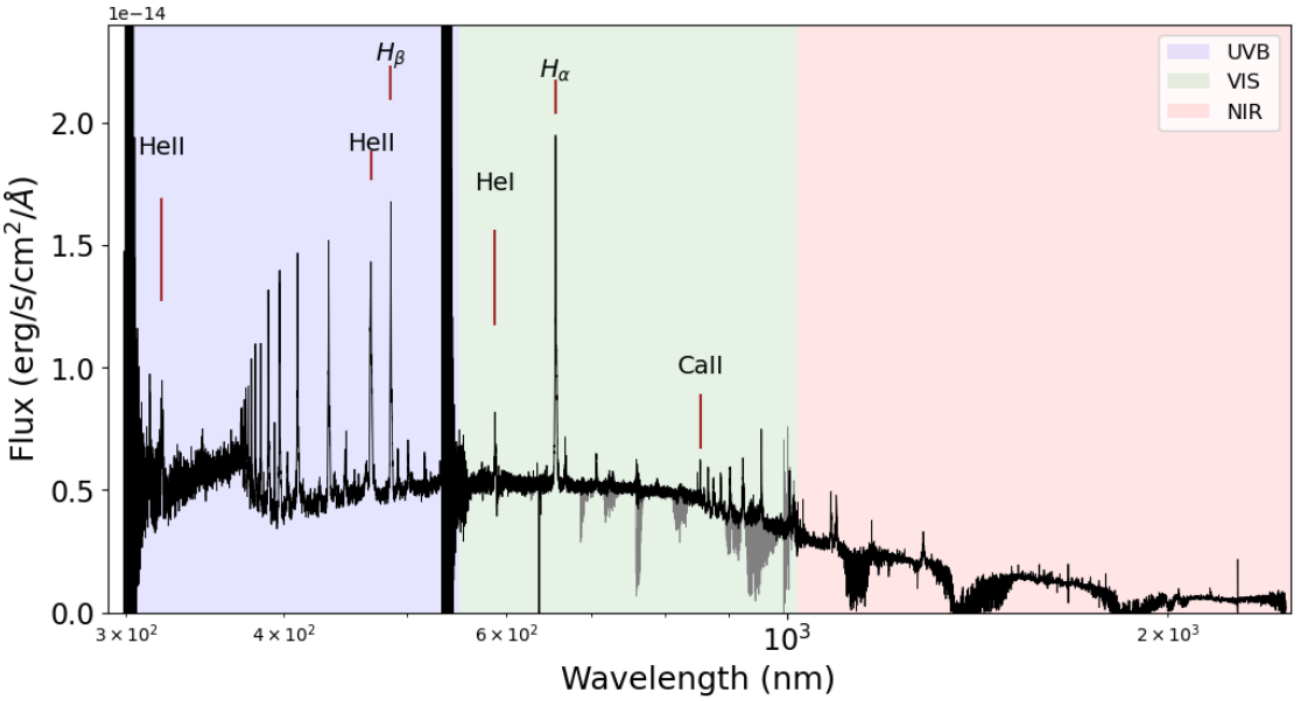

Figure 2.6: Spectrum of J194827-131733 with a log scale in wavelength showing the 3 arms of X-shooter (UVB, VIS, NIR), In the VIS arm, the grey line represent the spectrum with the telluric absortion. In black in the VIS arm is the spectrum corrected with *Molecfit*

sphere leads to the formation of telluric absorption lines in ground-based observatories. Correcting for these lines, usually relies on observations of specific stars obtained close in time and air mass to the science targets (Standard stars), or the same star can be used for correction. The second alternative, is more convenient to optimise the telescope time.

The scientific data retrieved from the ESO portal, which have undergone initial reduction by the ESOREFLEX pipeline, and it is optimal compared to the reduction perfomed in this work of the few first spectra. Therefore, I used the data retrieved fromt he ESO archive. However, it's important to note that these data do not include telluric correction. To address this, we utilize MOLECFIT, (Kotze, E. J. et al., 2016; Smette, A. et al., 2015), which is a tool to correct telluric absorption lines based on synthetic modelling of the Earth's atmospheric transmission radiation. Combines a radiative transfer code, comprehensive molecular line database, atmospheric profiles, to model the instrument line spread function. The atmospheric profiles are created by merging a standard atmospheric profile representative of a given observatory's climate, of local meteorological data, and of dynamically retrieved altitude profiles for temperature, pressure, and humidity, this data is obtained reading the header of the fits file.

ESOREFLEX employs an interactive panel allowing users to monitor the workflow progression. The Molecfit workflow steps is illustrated in Figure 2.7. In the first step, data is loaded by specifying the directory of the FITS file earmarked for telluric correction and selecting the directory of the output, if you want to reduce the SCIENCE file, you have to specify in the homepage of ESOREFLEX. A window within ESOREFLEX displays telescope name and FITS file details, prompting users to select specific files for reduction. After try and testing several parameters I develop a recipe

Table 2.3: Region selected to fit the telluric absorption lines, with a $\chi^2 \approx 1.4$ for the fitting procedure.

H_2O nm	O_2 nm
825.4 - 829.3	687.2 - 693.1
915.1 - 916.7	759.5 - 766.8

execution for all VIS files obtaining a $\chi^2 \approx 1.4$ for all files, (the χ^2 nearer to one, the better the fit is, and therefore the better the correction is).

Figure 2.7: Interactive EsoReflex enviroment running molecfit pipeline

Moving to step 2, Molecfit initiates atmospheric modelling based on header data, encompassing parameters such as pressure, humidity, location, and air mass. A subsequent window emerges, necessitating user selection of telluric absorption line regions. These regions must exclusively exhibit telluric activity for optimal model fitting. EsoReflex has a option to plot the telluric lines for different molecules, thus the user can observe the regions of high telluric absortion. Examples of the telluric bands of H_2O and O_2 are shown in figure 2.8. In this step you can "*rerun recipe*" to repeat the process until the user obtains an optimal χ^2 for the selected region. The specific regions utilised for reducing the VIS arm as a recipe are outlined in Table 2.3.

In Step 3, we construct the atmospheric transmission, referred to as "calctrans" in molecfit, which involves calculating the transmission function. Moving to Step 4, we apply this transmission function to perform the Telluric correction. The Telluric correction aims to remove or mitigate

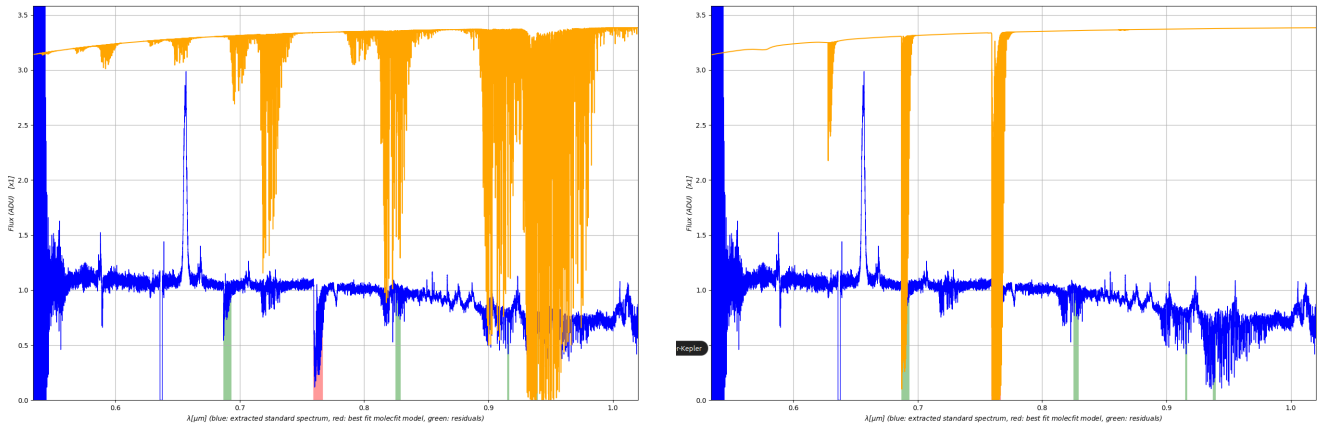

Figure 2.8: The orange lines represent the telluric absorption lines for H_2O and O_2. The H_2O lines are depicted on the right, while the O_2 lines are on the left. The blue spectrum corresponds to the scientific input, while the green regions denote the selected regions to fit the absorption band. The red region serves as a cautionary indication that fitting the telluric absorption is challenging, primarily due to significant band absorption.

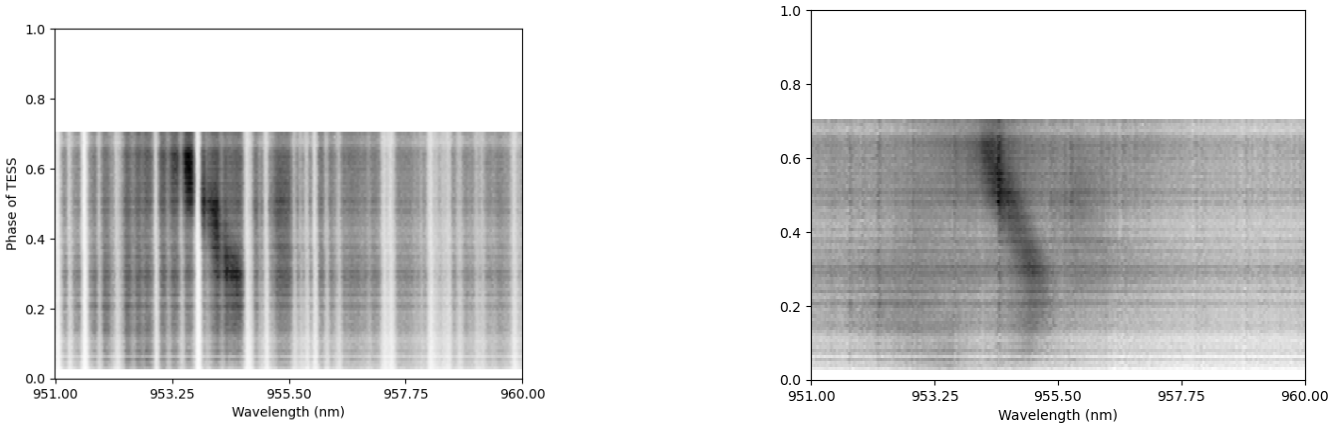

Figure 2.9: Trailed spectrum of the Paschen line at 954 nm, show the telluric correction done with Molecfit. From 0 to 1 in the y-axes is the phase of the system and in the x-axis is the wavelength in nanometres. Left image show the exposures without the telluric correction, in which the white vertical lines correspond to H_2O absorption. In the right is the result of the telluric correction.

the effects of atmospheric absorption lines from the observed spectra. By applying the calculated transmission function, we effectively compensate for the atmospheric distortions and obtain a corrected spectrum. Finally, in Step 5, we save the output in the directory specified earlier. In Figure 2.6 in grey is the spectrum with telluric lines and in black is the spectrum corrected.

The initial aim was to eliminate telluric lines from the NIR arm, with the objective of acquiring absorption lines in the three X-shooter arms. However, the NIR spectrum show problemtic regions. The regions 1250 nm - 1500 nm and 1750 nm to 2000 nm, the flux is nearly zero because of atmosphere absorption, as depicted in Figure 2.6, Consequently, when calculating the transmission function using the sensitivity function, which includes arrays of zeros in these problematic regions, dividing to correct the spectrum results in significant noise in the corrected spectrum. Therefore, the NIR spectra are not used in the analysis of this work.

To illustrate the correction of telluric lines, Figure 2.9 depicts the data before Molecfit processing on the left and after correction on the right. Prior to correction, the spectrum exhibited significant absorption bands attributed to atmospheric water vapor (H_2O). Through the correction process, these absorption features were mitigated, consequently aiding in the identification and elucidation of an emission line within the affected region.

The reduction process applied to the VIS file facilitates the identification of an OI absorption line (Figure 4.4) within the region of H_2O absorption lines before correction. This observation holds significance as it provides insight into the spectral characteristics of the data prior to correction. Furthermore, the reduction process enhances the suitability of the data for the cross-correlation analysis outlined in the Future Work section in which we need to find absorption lines suitable to apply this technique.

Chapter 3

Results

3.1 J194827-13173 an eclipsing polar

The X-shooter spectrum displays emission of Balmer and helium lines, however they are not doubled peaked, indicating the absence of an accretion disc, and thus the emission of these lines is produced in other region(s) of the system. Moreover, the detection of He II in the spectrum suggests the presence of an extremely hot region within the system. However, the absence of a disc leads us to exclude the possibility of a nova-like system, indicating instead that it is most probably a magnetic system. In addition, some of the spectra display flux variation in the optical range, which could be due to cyclotron harmonics humps approximate to phase 0.51 (i.e number 63 exposure)

Another argument arises from the periodicities identified in the Periodogram (See Figure 2.3), which display harmonics of the fundamental period. There is no evidence of the spin period of the white dwarf neither the beat period usually identified in the IPs (e.g. Bloemen et al., 2010). The single period display in the periodogram is caused by the eclipses observed in the lightcurve, and the presence of a single period suggests that the white dwarf rotates at the same rate as the orbital period. Hence, considering the magnetic nature, the absence of a disc, and a single period, I suggest that this CV is a polar.

3.2 Geometry of the system

Using the X-shooter spectra, I built trailed spectra of several emission and absorption lines. The trailed spectrum represents a 2D visualisation where the wavelength is plotted along the x-axis, while time or phase is depicted along the y-axis. This format enables the observation of the sinusoidal motion of absorption or emission lines attributed to various elements. Such motion results from the Doppler shift induced by orbital dynamics across different phases. This technique allows to track the variations in spectral lines over time or orbital phase, shedding light on the accretion processes, and orbital dynamics within the system as explain Hellier (2001). Figure 3.1 shows the trailed spectra for Balmer, Helium and Calcium lines. In addition, overplotted in orange or blue is shown a sinusoidal function defined as:

$$W = W_0 + A * \mathrm{Sin}\left(\frac{2\pi\ t}{P_{orb}} + \phi_0 * 2\pi\right) \tag{3.1}$$

Where W_0 the wavelength shift, A is the amplitude of the motion, t is the times of the observations, P_{orb} is the orbital period derived from *TESS*, and ϕ_0 is the offset of the sine in the y-axes. The phase equals zero is defined at the primary eclipse detected in the *TESS* lightcurve (see right panel in Figure 3.2). It is worth to mention that the sine curve is not a fit, it is just for display purposes, but it illustrates the offset different sine curves could have in reference to the phase. Table 3.1 lists a summary of the estimated offset for several lines.

With reference to the *TESS* light curve (Figure 2.2) and the dominant peak in the periodogram corresponding to the orbital period of $P_{orb} = 5.197 \pm 0.015$ hours, our initial approach involved calculating the number of eclipses between the observed eclipses by *TESS* and the closest eclipse in our observations. This analysis allowed us to extrapolate the *TESS* light curve, assisting in determining the system's phase zero during our observation. As the X-shooter observation are roughly one year far apart from the *TESS* observation. The progressive accumulation of errors in the determination of orbital periods has led to a significant offset. To address this, I calculated the number of eclipses that should have occurred between the final eclipse observed by TESS and our observations, arriving at a total of 1273 eclipses. By multiplying this count by the error associated with the period, I estimated a cumulative error of approximately 19.9 hours. It is important to note that this method inherently carries an error roughly equivalent to several times the orbital period itself. Indeed, the period needs revision, since the predicting eclipses in the *TESS* lightcurve based on the period, I notices there is an offset compared to the ones observed in the *TESS* lightcurve.

I attempted a different approach, I built an X-shooter light curve, to identified if the eclipse was observed or not troughtout the observations. In order to built the lightcurve, I integrated the X-shooter spectra ($f(\lambda)$) convolved by the *TESS* passband ($T(\lambda)$), i.e.

$$F = \frac{\int f(\lambda)T(\lambda)d\lambda}{\int T(\lambda)d\lambda} \tag{3.2}$$

Then I identified that the X-shooter captured the system exiting from the eclipse (which is also clearly seen in the trailed spectra of H_α, H_β in which the emission is absent). Using the initial and end times of the X-shooter observations, I determined the fraction that these observations cover troughtout one orbital period. I determined a fraction of approximately 0.666. Therefore, this prompts to accommodate the initial and final phases at approximately 0.03 and 0.70, respectively. The right panel of figure 3.2 shows the *TESS* lighrcurve in black and overplotted in grey (within the pink band) is demarcated the X-shooter lightcurve. An eclipse was observed at the beginning of the light curve. The light curve of X-shooter exhibits significant variability, notably characterised by a decay occurring around the 0.68 phase mark. However, the most notable variations are observed during the eclipse phase.

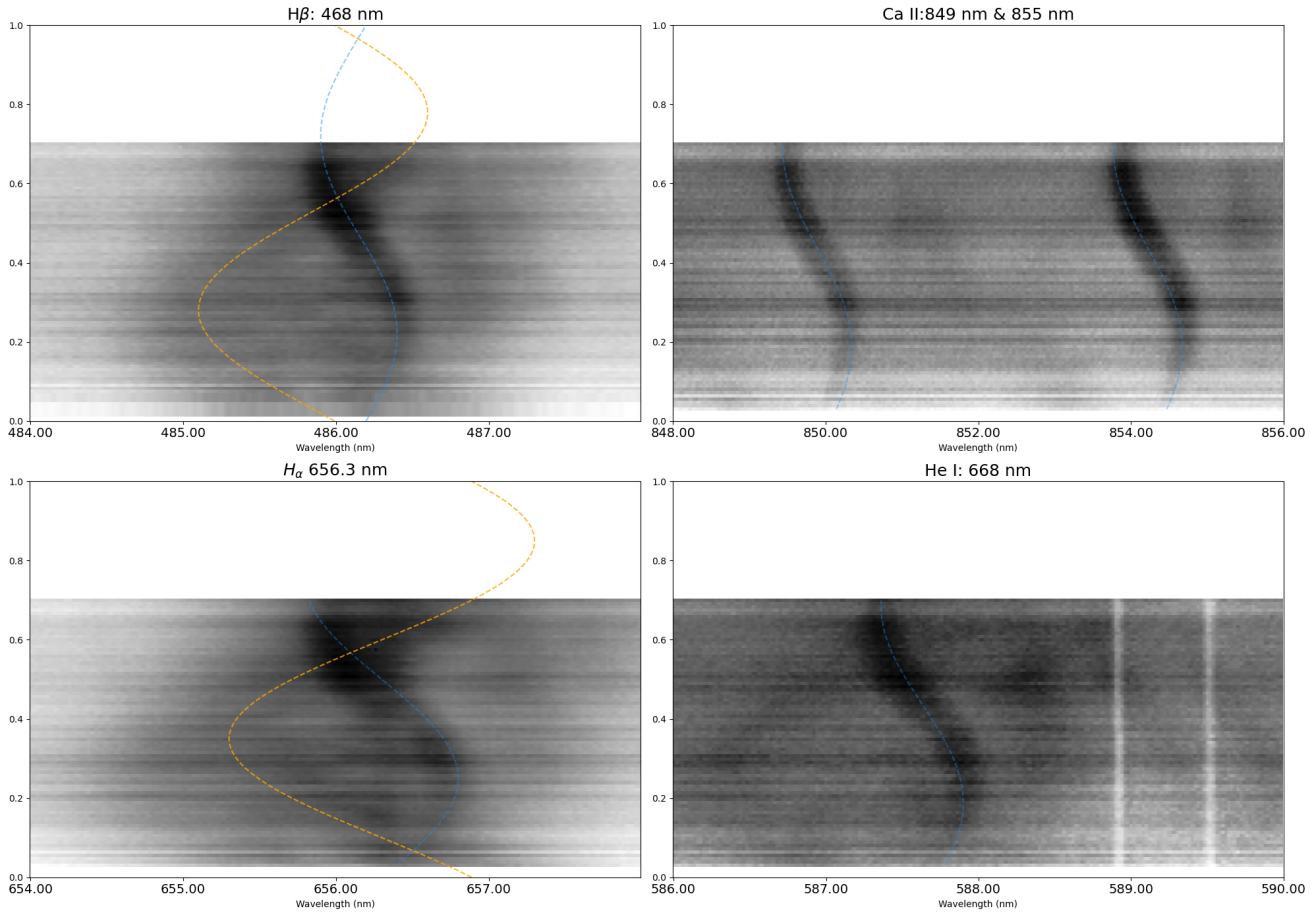

Figure 3.1: Trailed spectra of H_β (top left), H_α (bottom left), Ca II doublet (top right) and He I (bottom right). Some telluric absorption lines persist close to the He I line even after the application of telluric correction. I have identified these lines as the Na I doublet. Notably, the molecfit tool does not incorporate Na or Na-containing molecules for correcting these lines. The blue dashed lines represent emission lines originating from the irradiated hemisphere, while the orange lines stem from the accreting curtain and/or the magnetic stream.

Table 3.1: Summary of shift of every line of the trailed spectrum. Blue indicates the emission lines identified to originate from the donor's irradiated face, while orange signifies the shift of stream-like regions and curtain emission, particularly in the case of He II. The color scheme maintains coherence with Figure 3.1 and Figure 3.3, providing a visual reference for the observed shifts and their corresponding regions. The '*' in He II and He I shows a speculative structure that refers to the corresponding column, without a dashed plot in the Figures 3.1 and 3.3.

Line	**Shift (ϕ_0) Blue**	**Shift ϕ_0 Orange**
H_β	0.03	0.47
$H\alpha$	0.00	0.40
He I	0.01	*
He II	0.03*	0.49
Ca II	0.1	-

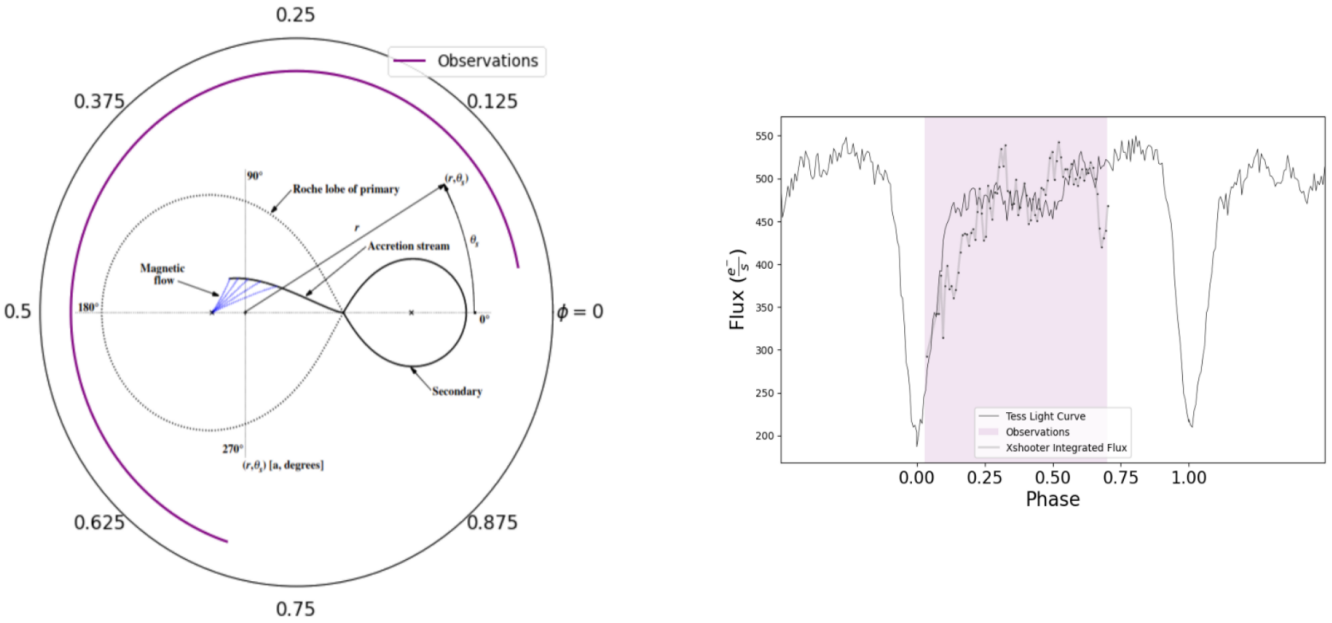

Figure 3.2: *Left:* a phase scheme is presented, where $\phi = 0$ signifies MS eclipsing the WD. The phases we observed are highlighted in purple, while the blue dotted line represents the phase during which the O I absorption line was visible (refer to Section 4.1). *Right:* the light curve of *TESS* depicting an arbitrary eclipse has been extrapolated to illustrate the section of the light curve in which the X-shooter observations were taken (pink band).

3.2.1 Irradiated face of the donor

The clear sinusoidal feature (dashed blue line) in the trailed spectra of H_α, H_β, He I, and Ca II behave similarly. In many magnetic CVs, H_α and H_β originates from the irradiated hemisphere of the donor star (e.g. Balman et al., 2024; Schwarz et al., 2005). If we assume this model in our system we should detect an increase line flux emission while the emitting region (i.e. the irradiated face) becomes visible along the line-of-sight, reaching a maximum close to a phase of 0.5, if not other source of emission is present in the system other than a symmetric irradiated area of the donor and the white dwarf does not block the irradiated face. The trailed spectra show a narrow sinusoidal feature demarcated by a dashed blue line in figure 3.1, which at a phase zero there is not emission and at a phase of approximately 0.22 the emission appears and moves away from us. Close to a phase of 0.5, the trailed spectra show a decrease of the emission line, which is more clear in the trailed spectrum of H_α (bottom left panel in Figure 3.1), which could suggest some other large structure (e.g. the ballistic stream, see section 3.2.2) that could have been blocking the irradiated face. When the irradiated face approaches to us, the line flux emission increases which could be that the irradiated face is not a symmetric region centred at the L1 Lagrange point, but it is displaced to the leading hemisphere of the donor (e.g. Szkody et al., 1999).

The Ca II emission line (shown at the top left in Figure 3.1) remains detectable across all phases during the X-shooter observations. However, its intensity notably diminishes near the eclipse phase, i.e. at phase zero. The shape of the line in the trailed spectra synchronises with the emission lines of H_α and H_β, leading to the conclusion that the emission originates from the

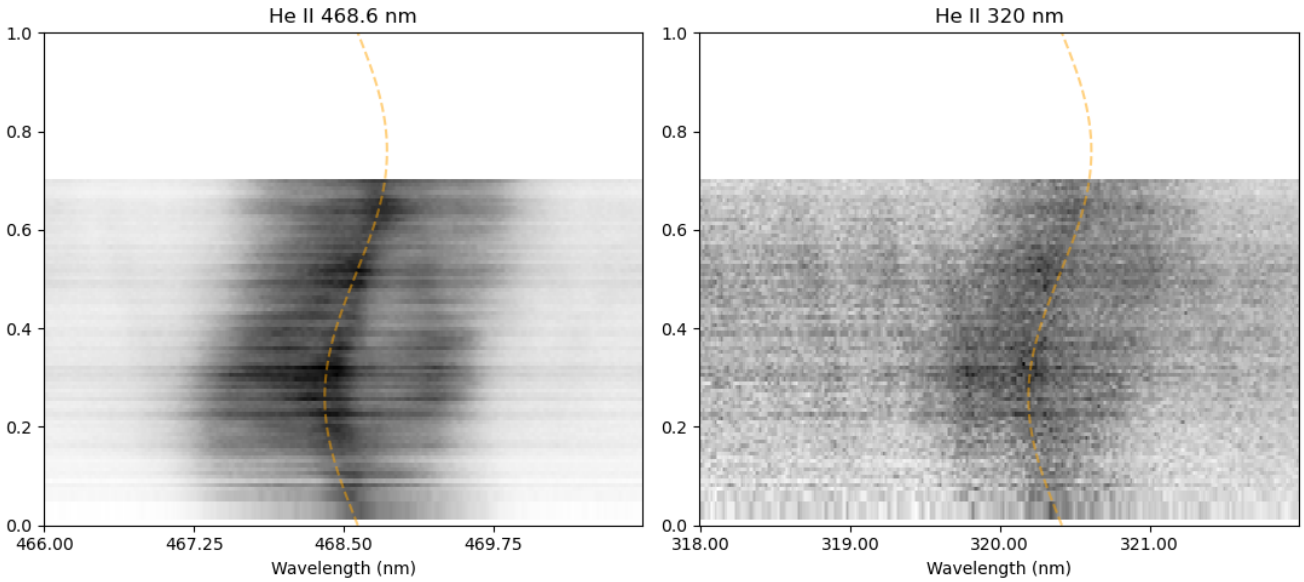

Figure 3.3: The accretion stream originating from the WD displays He II emission lines moving with a positive velocity, indicating a proximate region adjacent to the WD.

irradiated surface of the donor star.

Finally, the He I emission line also displays similar behaviour (see bottom right panel in Figure 3.1). Consequently, it is likely that He I originates in the irradiated region of the donor star, sharing behavioural characteristics with H_α, H_β and the Ca II lines.

H_β, Ca II, and He I are identified as Narrow Emission Line (NEL) spectra, and as we can mentioned, they likely originating from the irradiated hemisphere of the secondary star, as proposed by the model of Biermann et al. (1985). But, it is worth to note that H_α exhibits a larger amplitude and velocity dispersion, attributed to its generation within the stream itself (see next section). H_α emission arises from both the stream and the irradiated face, owing to its lower transition energy compared to other lines such as H_β.

3.2.2 Ballistic accretion stream

The trailed spectra of H_α, H_β and He I in addition display a large broad curved pattern with high velocities (dashed orange line in figure 3.1). Such features has been identified in previous works of magnetic CVs as a ballistic accretion stream leaving the donor (e.g Kotze, E. J. et al., 2016).

This broad H_α emission, depicted in orange, moves in antiphase with respect to the donor (i.e. $\phi \approx 0.40$). The H_α line exhibits larger amplitude than the emission from the irradiated face, attributable to its acceleration of the material in the stream by not only the gravitational potential but also the WD's magnetic field. For the H_β broad feature depicted in the top left of Figure 3.1, the observed behaviour mirrors that of the H_α line. At approximately a phase of 0.40 in the trailed spectra (Figure 3.1), the emission line originating from the stream adjacent to the WD overlaps with the emission line from the donor's irradiated region, resulting in an increased flux within this region of the trailed spectra.

3.2.3 He II emission coming from close to the white dwarf

He II emission lines have been observed in magnetic CVs may stem from both the accretion stream within the magnetosphere and the irradiated region of the donor star. The polar V1309 Ori, shows that the He II traces H_α, and the authors concluded that emission of He II is produced by the irradiated face of the donor (e.g. Staude, A. et al., 2001). In contrast, the asynchronous polar BY Cam (Schwarz et al., 2005) displays He II in anti-phase with H_β, which is similar to the systems analysed in this work. The authors suggest that the emission of He II comes from the proximity of the white dwarf, e.g. the magnetosphere.

The trailed spectra for the He II lines are shown in Figure 3.3. However, in our system, the scenario where the He II lines originate from the donor's irradiated region it is not the case. This is because the He II lines exhibit an offset of $\phi_0 \approx 0.49$ leading to positive velocities during the initial phases, contrary to what would be expected from the donor's lines, which should typically display redshifts until 0.5 phases. This configuration suggest that the He II is forming close to the white dwarf, i.e. at the magnetosphere.

Additionally, it lacks the discernible stream features observed in H_α and exhibits NEL. The broader profile of H_α is attributed to its emission across various regions of the stream with differing velocities, leading to line broadening. Similarly, He II (He II λ468.6 nm and He II λ320 nm) displays broadening which could be due to velocity dispersion within the curtain that hit white dwarf.

The other stream-like lines in orange (H_β have a shift of $\phi_0 \approx 0.47$), and $H_\alpha \approx 0.40$, therefore the closer to WD's orbit is the He II, for this reason I propose that the source is the curtain, instead H_β and H_α, it is emitting in the curtain and in a larger structure within the stream, causing a different ϕ_0 respect of He II.

The Light Curve show an augment in flux at 0.5 phase, respect to the eclipse that occur at 0 phase, is the MS eclipsing the WD and the irradiated hemisphere of the secondary then the MS stops blocking the WD (or the stream of the WD). At approximately phase 0.5, the process of revealing the irradiated phase of the secondary star begins. In the trailed spectrum analysis, it becomes evident that spectral regions featuring lines exhibiting negative radial velocities (redshift) are proximate to the MS, whereas those initially displaying positive velocities (blueshift) pertain to the WD.

Summary

In summary, the trailed spectra analysis yields several key insights:

Firstly, the absence of double-peaked emission lines suggests the absence of a disc structure. Instead, the observed structures can be attributed to streams.

Secondly, I provide an explanation for the phase-resolved spectroscopy, delineating three principal regions:

- The irradiated hemisphere of the donor, which exhibits a phase around ≈ 0.5 and manifests Narrow Emission Lines (NEL).
- The stream emission, which broadens the emission line and occupies a phase range of $\approx 0.4 - 0.47$. This broadening occurs due to the presence of differential velocities within the stream region, displaying greater velocities compared to the irradiated hemisphere.

- The accreting curtain, characteristic of polar systems, which follows the White Dwarf's (WD) orbit around $\phi_0 \approx 0.5$. Within this region, we identify He II emission occurring at approximately $\phi_0 \approx 0.49$. The He II line exhibits broad emission due to acceleration resulting from the magnetic field.

This categorisation provides a clearer understanding of the distinct spectroscopic features observed across different phases of the binary system.

For a deeper comprehension of the emission regions, it is essential to develop more intricate maps such as Doppler tomographs or inside-out maps (Schwarz et al., 2005; Bakowska et al., 2021; Kotze, E. J. et al., 2016). Nevertheless, these techniques entail greater complexity, and my intention is to further investigate this system.

Chapter 4

Discussion

4.1 Is J194827-131733 in low or high state?

Polar stars typically undergo fluctuations between low and high states (see section 1.3.4 for a plausible explanation of the cause of this phenomenon). Given the appearance of the X-Shooter spectra. i.e. the white dwarf and the donor are not detected. Most of the optical flux comes from the irradiated face of the donor combined with the accretion stream, therefore the system is undergoing a high accretion which suggest the system to be in high state.

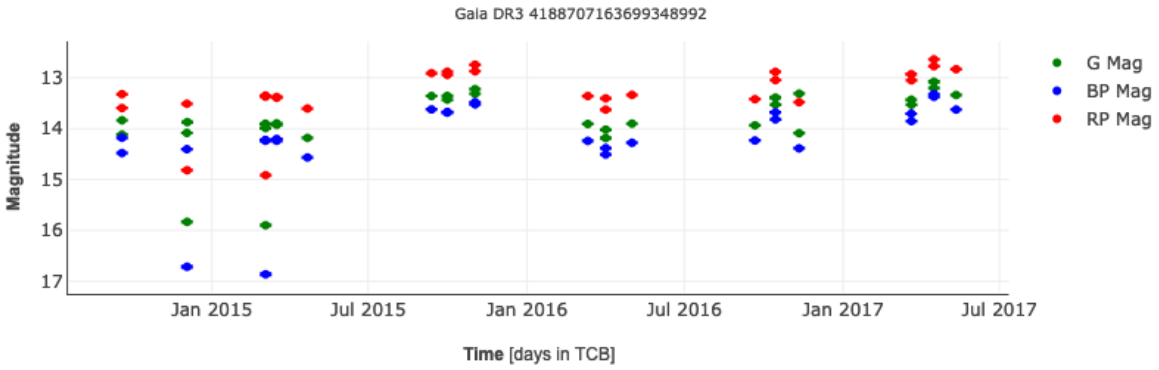

Figure 4.1: Multi-epoch *Gaia* photometry of J194827-131733

.

J194827-131733 was flaggued by *Gaia* as a variable object, and therefore there is multi-epoch *Gaia* photometry available. I have retrieved the *Gaia* photometry which covers of from January 2015 to July 2017. The light curves is shown in figure 4.1, which displays a clear dip between. The discernible change occurred between July 2015 and January 2016, where the magnitude decreased from 14 to nearly 13. So, it could be that the system underwent a short period of low state or the photometry was taken during one of the eclipses. While such transitions are more common in polar systems, long term photometric monitoring is needed to confirm is the system experiences low mass transfer episodes. To achieve this goal, observing time has been allocated with SPECULOOS (Principal Investigator: Meza) to collect optical photometry data throughout the first semester of 2024.

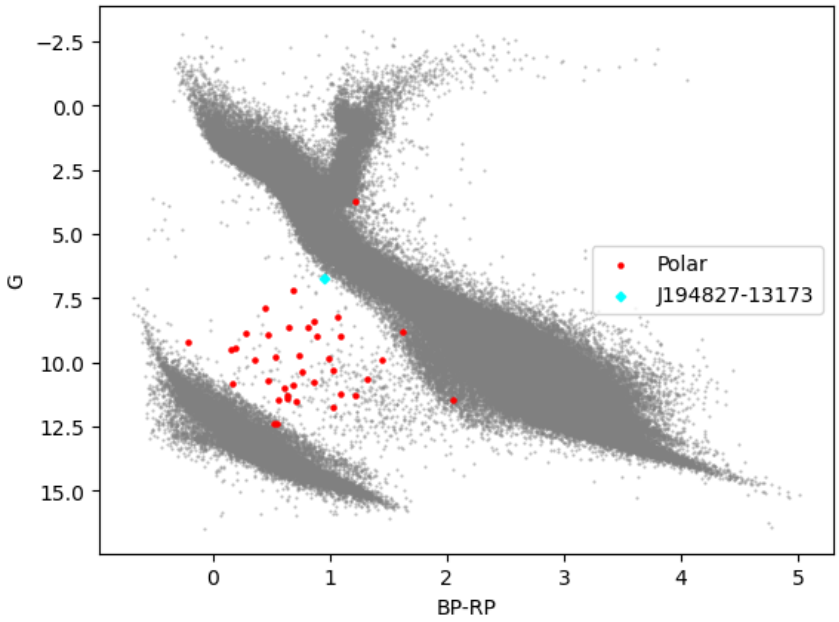

Figure 4.2: Diagram HR, gray dots are Gaia object within 200 pc, red object are Polars obtained in Inight et al. (2023), cross match with Gaia photometry. Obtaining 40 + 1 polars containing J194827-131733.

I constructed an *Gaia* HR diagram illustrated in Figure 4.2, by crossmatching the catalogo of Inight et al. (2023) with *Gaia* data release 3. Following this process, 40 polar stars (red dots), along with one additional star, J194827-131733 (cyan dot) stands out from the population due to its high optical luminosity, which could be due to its high accretion rate.

In the low state of the system, the opportunity arises to study the White Dwarf (WD) in its naked form. This is evident in the spectrum depicted in Figure 2.6, where the WD is not distinctly visible.

4.2 The magnetic field

As it has been suggested earlier, the system is likely to be a polar CV, and for instance its magnetic field should be higher than 10 MG. In the corrected spectrum shown in black in Figure 2.6, the presence of cyclotron bumps is not distinctly evident. While there may be some indication of their presence in the 250-500 nm range, the observation lacks clarity in this regard. Additionally, the spectrum does not exhibit a prominent WD spectrum in the UVB region; either it is too weak or potentially obscured by other factors such as the accretion stream.

The monitoring program outlined in the previous section (section 4.1) will serve to identified when the system enter a phase of low-state, which will facilitate to detect the white dwarf and maybe the presence of Zeeman splitting of the Balmer lines (e.g. Fuchs et al., 2016).

4.3 Precession of magnetic white dwarf pole?

Our accretion model comprises a ballistic stream (see Figure 3.2) and a curtain pointing in Z direction, following magnetic lines in the magnetosphere region, and a stream. We propose a irradiated phase of the secondary with a $\phi_0 \approx 0$ based of the presence of NEL. And a magnetic stream falling to the WD originating He II in a curtain with $\phi_0 \approx 0.49$. And the other stream-like emission in orange 3.1, have broad emission lines and high velocities. Another final component of our model includes both the inclination of our point of view and the inclination of the magnetic pole of the white dwarf.

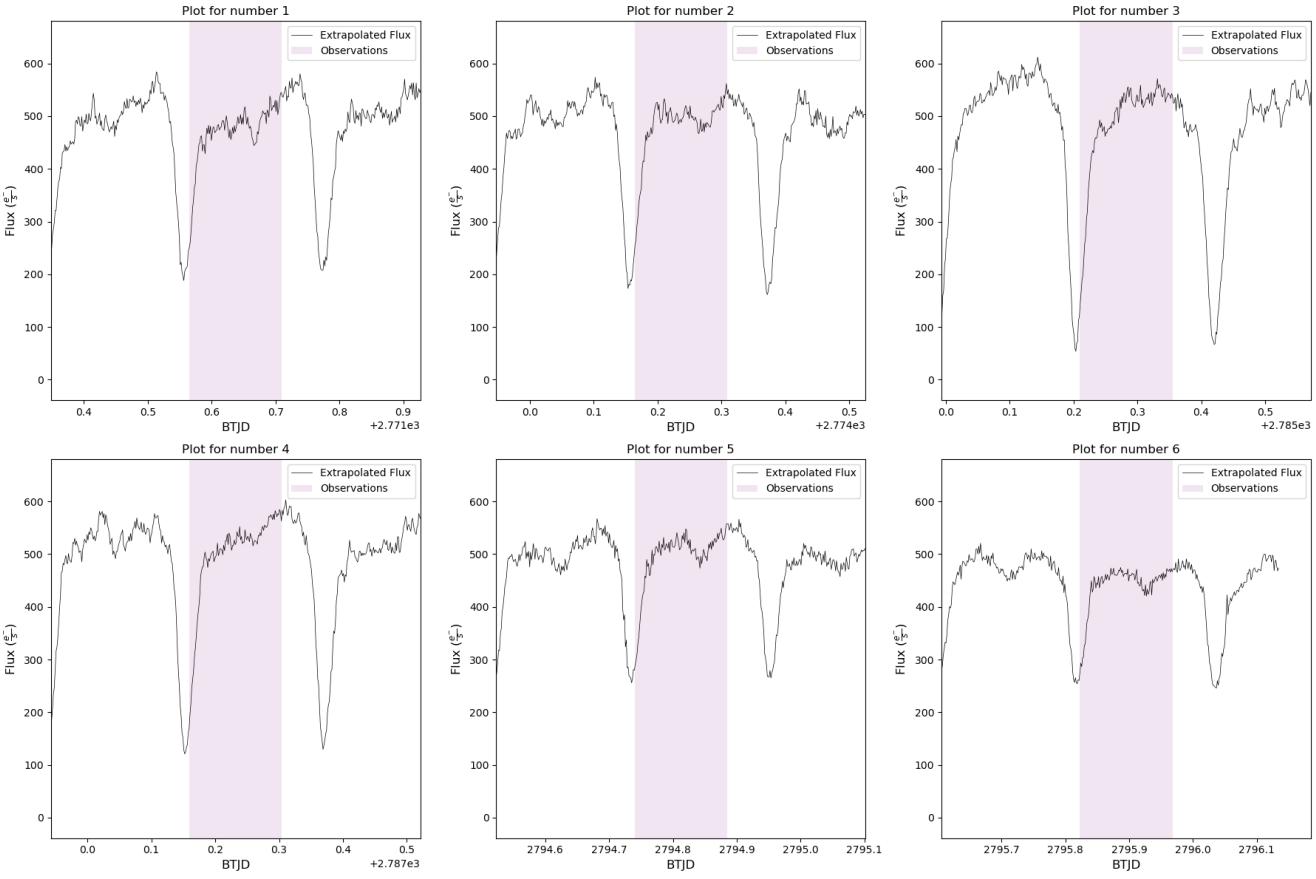

Figure 4.3: Zoom of the eclipses in Figure 2.2, evidence variability inter eclipses.

Figure 4.3 displays six different snapshots of the *TESS* lightcurves, which display different shapes between the eclipses on timescales of days which could be a result of a change of the magnetic poles.

An inclination of the pole of accretion not only causes the accretion disc to tilt but also results in the inclination of the associated curtain, as demonstrated by Romanova et al. (2003). By creating a 3D simulation of an accretion disc with an inclined dipole, it becomes evident that the curtain also inclines. Romanova et al. (2004) analised the inclination of the accretion (Θ) and inclination of the line-of-sight (i), and predict the shape of the lightcurves based on their a pole accretion model. Their predictions show similarities to some of the shapes identified in the *TESS* lightcurve

of J194827-131733: A combination of $i = 75°$ $\Theta = 15°$ or the combination $i = 75°$, $\Theta = 45°$ in their model is able to emulate the snapshot number 1 and number 4, respectively that are shown in Figure 4.3.

If the magnetic pole is undergoing some sort of precession, as a result, the stream undergoes morphological changes and may also irradiate the secondary, leading to asymmetries in the irradiated region. This configuration adds complexity and intricate results to the light curve. For instance, in cases where the stream must follow a much larger trajectory due to an inclination in the magnetic pole, it is possible that at 0 phases, the stream may not be eclipsed. Subsequently, the same stream can eclipse a region in the irradiated hemisphere of the secondary, causing the mid-depression observed in light curves number 1, 5, and 6 at approximate 0.5 phases. However, further research is needed to confirm this speculation.

4.4 Detection of absorption of O I

After applying the telluric correction, an interesting observation emerged: the appearance of the O I triplet at 777.2/777.4/777.5 nm. The trailed spectrum surrounding the O I line is shown in left panel in Figure 4.4, revealing a broad feature at the beginning of the X-shooter observations that subsequently disappears at a phase of roughly 0.25. In certain eclipsing polar systems, it has been observed that emission lines briefly transition into absorption, potentially explained by the passage of a curtain in front of the white dwarf (e.g. Rodriguez et al., 2023) as illustrated in the right panel of Figure 4.4. However, in this case, this could not explain the short appearance of the absorption, given that none of the hydrogen lines which are in emission, turns into absorption when this happens. In addition, I can identified another absorption feature of O I which persist and traces the motion of H_α, which could be absorption from the donor's photosphere, and hence a potential feature to determine the amplitude radial velocity of the donor.

4.5 J194827-131733 within the Polar population

The CV population exhibits two distinct features in its period distribution. Firstly, there's a gap observed between 2-3 hours (Schreiber et al., 2024), believed to result from the decrease in magnetic braking of the donor star once it becomes fully convective (Knigge et al., 2011). Secondly, there's a period minimum around 70 minutes, thought to occur when the donor star becomes quasi-degenerate.

The evolution of polars differs significantly from that of non-magnetic CVs due to the influence of the WD magnetic field on magnetic braking. Two primary evolutionary models address these changes in polars: the enhanced MB model (Hameury et al., 1989) and the reduced MB model (Li et al., 1994; Webbink & Wickramasinghe, 2002). In the enhanced MB scenario, the magnetic field lines of the WD trap the wind from donor, leading to an increase in the magnetosphere radius. This results in enhanced angular momentum loss via MB, causing accelerated mass transfer and shorter evolutionary time scales. In some instances, mass transfer may become thermally unstable, leading to a very brief lifespan for these systems. Conversely, in the reduced MB scenario, the MS donor's winds carry away less angular momentum compared to the non-magnetic case, as part of the wind remains trapped within the system due to the strong WD magnetic field. So, here I explore how the period distribution of polars differs from that of non-magnetic CVs.

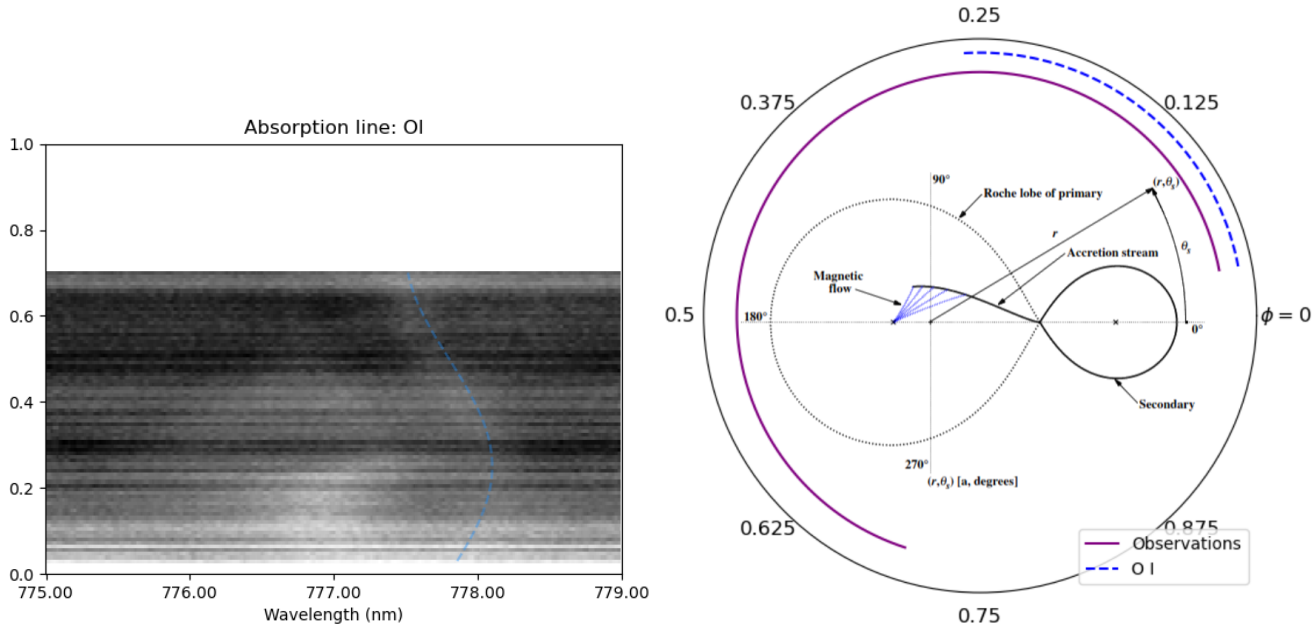

Figure 4.4: *Left:* Absorption line of O I, which the one that persist is highlighted with a blue dashed line, and it is suggested that this line comes from the donor, while the broad absorption feature on the left might be the material we see trough the accretion curtain. *Right:* A schematic cartoon illustrating the accretion model that shows the phases (indicated by a dashed purple line) during which the accretion curtain absorbs O I.

.

Given the that SDSS is able to provide homogeneous samples, I retrieve all the polar systems from the the CV catalogue of Inight et al. (2023). In total, there are 65 polars. Adding the new polar J194827-131733 exhibited a 5.19-hour period. Intriguingly, we observed that this newly identified pola manifested at the long period domain in the histogram 4.5, making this system very interesting for follow up studies. Population synthesis studies on polars (Belloni et al., 2020) indicate that these systems gradually fill the 2-3 hour gap due to the reduction of angular momentum loss through magnetic braking. However, this study reveals a bimodal period distribution (their Figure 3) with a notable absence of polar systems around the 3-hour mark. J194827-131733 lies on the right side of this bimodality (see Figure 4.5).

J194827-131733 stands out among the other polar stars due to its notably high luminosity (Figure 4.2). If classified as a polar system, its parameters appear to deviate from typical expectations, exhibiting a longer period and ranking as the second brightest polar within the Gaia-SDSS cross-match dataset. Therefore making J194827-131733 and ideal target for multi-wavelength studies.

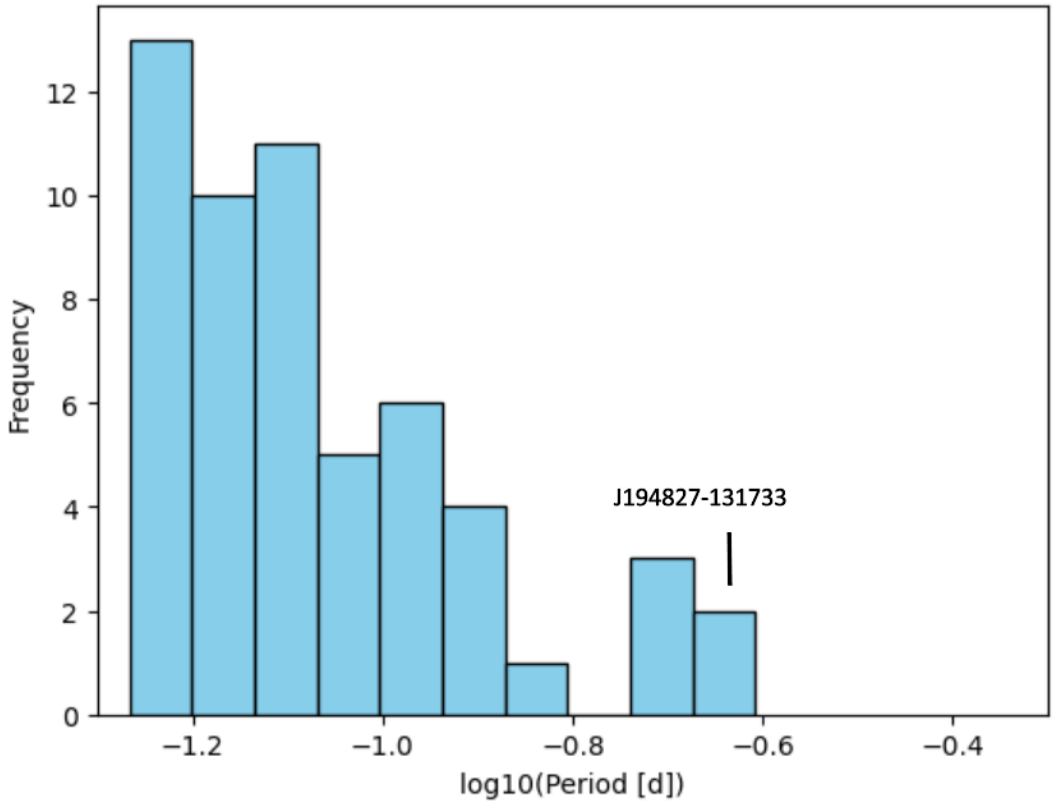

Figure 4.5: Period distribution of polar systems taken from Inight et al. (2023)

Chapter 5

Future Work

In this section, I will summarise the following steps regarding this work:

- Characterisation of the system

  The X-shooter spectra cannot be adequately fitted using composite models combining M-type stars and white dwarf templates because the stars are not directly visible. However, by utilizing absorption (i.e O I) features generated by the donor star, it becomes possible to measure the amplitude of the donor's radial velocity (using cross-correlation techniques). This method places constraints on the masses of the stellar components. Of particular interest is determining the mass of the white dwarf to ascertain whether it is more massive than its non-magnetic counterpart.

- Hunting the low state of J194827-131733:

  As speculated, this polar may have experienced a phase of low state. During such phases, the white dwarf (and donor) become discernible, facilitating a more precise characterization of both the white dwarf and donor stars. Additionally, if the white dwarf exhibits Zeeman splitting, the magnetic field can be determined. My approved proposal for SPECULOOS observation of J194827-131733 aims to monitor these potential changes.

- Measuring the accretion rate:

  Material falling radially experiences a significant adiabatic shock at a certain distance above the surface. This shock heats the infalling plasma to temperatures reaching several tens of keV, which subsequently cools through thermal plasma radiation at X-ray wavelengths and optical cyclotron radiation (Cropper, 1990). The X-ray spectra of polars are effectively characterized by a plasma with a multi-temperature and variable density structure (e.g. Cropper, 1990). Polars play a crucial role in understanding various processes, including mass transfer in the presence of strong magnetic fields, the generation of strong magnetic fields in close binaries, and the final stages of stellar evolution in the presence of intense magnetic fields. Utilising X-ray analysis (either *Chandra* or *XMM*) I aim to measure the accretion rate as demonstrated by Ok & Schwope (2022).

- Doppler tomography

With the purpose of having more information of the system we could make a doppler tomography of J194827-131733, elucidating and testing our accretion model. It would be a opportunity to see what is the truly nature of the H_β and He II disphase, that in the majority of the cases in the literature of polar (AM Her) the two lines are orbiting in the same phase because the source of both is the irradiated hemisphere of the secondary.

Chapter 6

Conclusion

In conclusion, J194827-131733 emerges as a mCV following detailed analysis of phase-resolved spectroscopy and long term, high-cadence photometry with *TESS*. This investigation, part of a broader program aimed at compiling a comprehensive sample within 500 pc, builds upon the work initiated by Pala et al. (2020).

Through analysis of the *TESS* light curve, J194827-131733 was identified as an eclipsing CV, enabling the extraction of its period, estimated at 5.197 ± 0.015 hours based on the most prominent peak in the periodogram.

The X-shooter spectra display numerous emission lines of hydrogen and helium, each with a single peak, indicating the absence of a disk. Consequently, this rules out the system being either a nova-like or an IP system.

My X-shooter observations cover 67% of the orbital period, ranging from the phases 0.03 to 0.7. Using trailed spectra, I identified that the system contains a donor which is highly irradiated producing emission of the Balmer lines an neutral helium. The spectra revels the presence of He II with a offset of $\simeq$0.5 in phase, which is contrast to some polars which is also produced in the irradiated face, the emission of this feature is most likely to be produce very close to the white dwarf, e.g. the magnetophere.

Additionally, the trailed spectrum of Hβ, Hα, and He I revealed structures orbiting as broad emission lines in anti-phase relation with the irradiated face of the secondary, indicative of emission from the magnetic stream. This leads to the conclusion of a ballistic accretion geometry, which explains the properties observed in the trailed spectrum analysis.

There is also find variations in the TESS light curve of J94827-131733 may be attributed to an inclination of the accretion pole, leading to constant variations in the stream and intricate interactions stretching the stream that could eclipse the irradiated hemisphere of the secondary, and also could cause asymmetries in the irradiated phase of the secondary.

Future work entails calculating essential parameters of the system, including the masses of the secondary and primary, as well as the strength of the magnetic field.

Bibliography

Abbott B. P., et al., 2016a, ApJS, 227, 14

Abbott B. P., et al., 2016b, ApJ, 832, L21

Astropy Collaboration et al., 2022, ApJ, 935, 167

Bakowska K., Marsh T. R., Steeghs D., Nelemans G., Groot P. J., 2021, A&A, 645, A114

Balman Ş., 2020, Advances in Space Research, 66, 1097

Balman Ş., et al., 2024, arXiv e-prints, p. arXiv:2401.06001

Barrett P. E., Chanmugam G., 1984, MNRAS, 210, 15P

Belloni D., Schreiber M. R., 2023, Formation and Evolution of Accreting Compact Objects. Springer Nature Singapore, p. 1–90, doi:10.1007/978-981-16-4544-0˙98-1, http://dx.doi.org/10.1007/978-981-16-4544-0_98-1

Belloni D., Schreiber M. R., Zorotovic M., Iłkiewicz K., Hurley J. R., Giersz M., Lagos F., 2018, Monthly Notices of the Royal Astronomical Society, 478, 5626

Belloni D., Schreiber M. R., Pala A. F., Gänsicke B. T., Zorotovic M., Rodrigues C. V., 2020, MNRAS, 491, 5717

Beuermann K., Reinsch K., 2008, A&A, 480, 199

Biermann P., et al., 1985, ApJ, 293, 303

Bloemen S., Marsh T. R., Steeghs D., Østensen R. H., 2010, MNRAS, 407, 1903

Charbonneau P., MacGregor K. B., 1997, ApJ, 486, 502

Cropper M., 1990, Space Sci. Rev., 54, 195

Ferrario L., de Martino D., Gänsicke B. T., 2015, Space Sci. Rev., 191, 111

Fuchs J. T., et al., 2016, MNRAS, 462, 2382

Halpern J. P., 2024, arXiv e-prints, p. arXiv:2402.00661

Hameury J. M., King A. R., Lasota J. P., 1989, MNRAS, 237, 845

Hellier C., 2001, Cataclysmic Variable Stars

Hessman F., Gänsicke B., Mattei J., 2000, Astronomy and Astrophysics, 361, 952

Higgins M. E., Bell K. J., 2023, AJ, 165, 141

Howell S. B., 2004, in Vrielmann S., Cropper M., eds, Astronomical Society of the Pacific Conference Series Vol. 315, IAU Colloq. 190: Magnetic Cataclysmic Variables. p. 353 (arXiv:astro-ph/0302368), doi:10.48550/arXiv.astro-ph/0302368

Imamura J. N., Durisen R. H., Lamb D. Q., Weast G. J., 1987, ApJ, 313, 298

Inight K., et al., 2023, MNRAS, 524, 4867

Kalomeni B., 2012, MNRAS, 422, 1601

Knigge C., Baraffe I., Patterson J., 2011, The Astrophysical Journal Supplement Series, 194, 28

Kolbin A. I., Suslikov M. V., Kochkina V. Y., Borisov N. V., Burenkov A. N., Oparin D. V., 2024, Astronomy Letters, 49, 475

Kotze, E. J. Potter, S. B. McBride, V. A. 2016, A&A, 595, A47

Kraft R. P., 1967, ApJ, 150, 551

Latham D. W., Liebert J., Steiner J. E., 1981, ApJ, 246, 919

Li J. K., Wu K. W., Wickramasinghe D. T., 1994, MNRAS, 268, 61

Liebert J., Stockman H. S., 1985, in Lamb D. Q., Patterson J., eds, Cataclysmic Variables and Low-Mass X-ray Binaries. p. 151, doi:10.1007/978-94-009-5319-2˙20

Littlefield C., Garnavich P., Mukai K., Mason P. A., Szkody P., Kennedy M., Myers G., Schwarz R., 2019, ApJ, 881, 141

Littlefield C., et al., 2023, AJ, 165, 43

MacGregor K. B., Charbonneau P., 1997, ApJ, 486, 484

Mukai K., 2017, PASP, 129, 062001

Ok S., Schwope A., 2022, A&A, 662, A116

Osaki Y., 1974, PASJ, 26, 429

Paczyński B., 1967, Acta Astron., 17, 287

Pala A. F., et al., 2020, MNRAS, 494, 3799

Patterson J., Price C., 1981, PASP, 93, 71

Ricker G. R., et al., 2014, Journal of Astronomical Telescopes, Instruments, and Systems, 1, 014003

Rodriguez A. C., et al., 2023, ApJ, 945, 141

Romanova M. M., Ustyugova G. V., Koldoba A. V., Wick J. V., Lovelace R. V. E., 2003, ApJ, 595, 1009

Romanova M. M., Ustyugova G. V., Koldoba A. V., Lovelace R. V. E., 2004, ApJ, 610, 920

Schatzman E., 1962, Annales d'Astrophysique, 25, 18

Schmidt G. D., Liebert J., Stockman H. S., 1995, ApJ, 441, 414

Schreiber M. R., Zorotovic M., Wijnen T. P. G., 2015, Monthly Notices of the Royal Astronomical Society: Letters, 455, L16

Schreiber M. R., Belloni D., Schwope A. D., 2024, A&A, 682, L7

Schwarz R., Schwope A. D., Staude A., Remillard R. A., 2005, A&A, 444, 213

Shears J., 2021, British Astronomical Association Variable Star Section Circular, 187, 9

Smette, A. et al., 2015, A&A, 576, A77

Staude, A. Schwope, A. D. Schwarz, R. 2001, A&A, 374, 588

Szkody P., Vennes S., Schmidt G. D., Wagner R. M., Fried R., Shafter A. W., Fierce E., 1999, ApJ, 520, 841

Verbunt F., Zwaan C., 1981, A&A, 100, L7

Warner B., 1995, Cataclysmic variable stars. Vol. 28

Warner B., 2003, arXiv e-prints, pp astro–ph/0310243

Webb N., Naylor T., Jeffries R., 2002, The Astrophysical Journal, 568, L45

Webbink R. F., Wickramasinghe D. T., 2002, MNRAS, 335, 1